Time-Varying Empirical Probability Densities of Southern Ocean Surface Winds: Linking the Leading Mode to SAM and Quantifying Wind Product Differences

MOMME C. HELL,[a] BRUCE D. CORNUELLE,[a] SARAH T. GILLE,[a] AND NICHOLAS J. LUTSKO[a]

[a] *Scripps Institution of Oceanography, University of California, San Diego, La Jolla, California*

(Manuscript received 7 August 2020, in final form 23 March 2021)

ABSTRACT: Southern Ocean (SO) surface winds are essential for ventilating the upper ocean by bringing heat and CO_2 to the ocean interior. The relationships between mixed layer ventilation, the southern annular mode (SAM), and the storm tracks remain unclear because processes can be governed by short-term wind events as well as long-term means. In this study, observed time-varying 5-day probability density functions (PDFs) of ERA5 surface winds and stresses over the SO are used in a singular value decomposition to derive a linearly independent set of empirical basis functions. The first modes of wind (72% of the total wind variance) and stress (74% of the total stress variance) are highly correlated with a standard SAM index ($r = 0.82$) and reflect the SAM's role in driving cyclone intensity and, in turn, extreme westerly winds. The joint PDFs of zonal and meridional wind show that southerly and less westerly winds associated with strong mixed layer ventilation are more frequent during short and distinct negative SAM phases. The probability of these short-term events might be related to midlatitude atmospheric circulation. The second mode describes seasonal changes in the wind variance (16% of the total variance) that are uncorrelated with the first mode. The analysis produces similar results when repeated using 5-day PDFs from a suite of scatterometer products. Differences between wind product PDFs resemble the first mode of the PDFs. Together, these results show a strong correlation between surface stress PDFs and the leading modes of atmospheric variability, suggesting that empirical modes can serve as a novel pathway for understanding differences and variability of surface stress PDFs.

KEYWORDS: Southern Ocean; Annular mode; Wind stress; Atmosphere-ocean interaction; Extratropical cyclones; Principal components analysis

1. Introduction

The Southern Ocean (SO) governs the global ocean uptake of anthropogenic heat and CO_2 (Gnanadesikan 1999; Swart et al. 2018; Gruber et al. 2019), and projections of future climate change depend on our of understanding SO ventilation (Sabine et al. 2004; Boé et al. 2009; Kuhlbrodt and Gregory 2012; Soloviev and Lukas 2013; Flato et al. 2013), trends in water mass transformation (Roemmich et al. 2015; Haumann et al. 2016), and mode water formation (Hanawa and Talley 2001; Naveira Garabato et al. 2009; Holte et al. 2012; Gao et al. 2018; Cerovečki et al. 2019). Changes in the SO mixed layer are largely driven by a combination of surface stresses and atmosphere–ocean heat fluxes, which together ventilate the upper ocean through stirring and mixing, with the strongest ventilation during intermittent and highly variable events.

The strong link between surface winds and ventilation of the SO mixed layer (ML) suggests that the southern annular mode (SAM), as the leading-order mode of the Southern Hemisphere atmospheric variability (Thompson and Wallace 2000), impacts long-term mixed layer changes (Meijers et al. 2019; Cerovečki et al. 2019). However, it remains unclear how large-scale month-to-month atmospheric variability drives short-term intense wind events under storms (Risien and Chelton 2008; Lin et al. 2018). This paper explores how short-term wind and stress variability relate to SAM, how they vary in time, and how well they are represented in observational products.

SO flux buoy observations suggest that only a few episodic wind extremes (>12 m s^{-1} or so) per year are responsible for most ventilation and deepening of the mixed layer (Schulz et al. 2012; Ogle et al. 2018; Bharti et al. 2019; Tamsitt et al. 2020), and similar intermittent effects emerge in other regions and model studies as well (Giglio et al. 2017; Whitt et al. 2019). Because the strength of mixing is also sensitive to the ocean mixed layer stratification, it remains unclear when mixed layer ventilation is more sensitive to mechanical wind forcing and when it is more sensitive to to surface heat fluxes. In both cases, strong mixing may be associated with extreme winds that are embedded in larger, more persistent wind patterns extending over hundreds of kilometers under extratropical storms. Rare high-wind (or high-stress) events under storms initiate highly nonlinear processes that transfer energy from the wind-generated waves to the upper ocean (Phillips 1985) and eventually to the large-scale flow. Extreme winds initiate a cascade of complex processes that influence mixing far beyond the location where they occur (Cavaleri et al. 2012).

Extremes in Southern Ocean surface winds are difficult to observe. The severe weather and lack of access to the region around Antarctica limit in situ observations and make remote sensing the dominant technique for recording surface winds. Satellite scatterometers observe surface capillary waves (centimeter-scale surface roughness) that are used to estimate the local 10-m surface winds (Atlas et al. 2011). However, the sparseness of in situ SO observations has impeded the calibration of remote sensing estimates for high wind speeds (Bourassa et al. 2019). In particular, a lack of observations of extreme winds under

Supplemental information related to this paper is available at the Journals Online website: https://doi.org/10.1175/JCLI-D-20-0629.s1.

Corresponding author: Momme C. Hell, mhell@ucsd.edu

DOI: 10.1175/JCLI-D-20-0629.1

cyclones and gaps in our knowledge of air–sea coupling under severe conditions make biases potentially largest where the winds are strongest (Rascle et al. 2008; Ardhuin et al. 2010; Chawla et al. 2013). These biases might correspond to differences between assimilated atmospheric reanalysis models (Wen et al. 2019; Ramon et al. 2019; McDonald and Cairns 2020), or between estimates of heat and momentum fluxes to the ocean (Bidlot et al. 2002; Cavaleri 2009; Li et al. 2013; Bourassa et al. 2013; Yagi and Kutsuwada 2020), and they can lead to biases in ocean forcing or upper-ocean mixing (Li et al. 2016; Taboada et al. 2019). All of these processes affect the assessment of the total wind energy input to the ocean (Rascle et al. 2008; Ferrari and Wunsch 2010).

Given the difficulties in observing surface winds, how certain can we be about surface stresses? Momentum transfer to the upper ocean relies on a variety of nonlinear processes that are driven by instabilities (surface wave growth, wave–wave interaction, conversion of near-inertial waves) and often involve turbulence (e.g., Phillips 1957; Miles 1960; Hasselmann and Hasselmann 1985; Asselin and Young 2020). A common way of parameterizing the transfer of momentum from the atmosphere to the ocean is calculating a surface stress vector $\boldsymbol{\tau}$ using the standard drag formula

$$\tau = \rho_a C_d |\mathbf{u}_{10}| \mathbf{u}_{10}, \tag{1}$$

where ρ_a is the density of air, and $\mathbf{u}_{10}$ is the 10-m wind vector. The drag coefficient C_d depends on wind speed $|\mathbf{u}_{10}|$, the ocean's sea state (surface wave spectrum), and the stratification of the atmospheric boundary layer (Fairall et al. 2003; Edson et al. 2013). Independent of the complex physics included in C_d, the transfer of momentum (i.e., surface stress) has at least a quadratic dependence on the wind speed magnitude $|\mathbf{u}_{10}|$, while the transfer of energy generally has a cubic dependence. Hence, variability in $\mathbf{u}_{10}$ has nonlinear impacts on fluxes of momentum and kinetic energy to the SO's surface (Simmonds et al. 2005).

The goal of the present study is to characterize the surface wind and stress over the SO in light of the complex relations between the surface stress and wind vector. We will use the time-varying probability density functions (PDFs) of surface stress and wind to understand their relation without assuming particular PDF shapes.

Surface winds on typical atmosphere model scales [daily time scales and $O(100)$ km length scales] are often characterized entirely by their mean and standard deviation. Hence, they are handled as Gaussian distributions defined by averaged quantities of the model output that is used to force the ocean. Wentz et al. (1984) and Wanninkhof (1992, 2014) describe the commonly used approach of using time-averaged quantities to estimate parameters of a Weibull distribution for the surface wind speed in each grid cell, which is then used to model air–sea fluxes. However, a number of studies have shown that surface stress depends on more than just the mean surface wind vector and its standard deviation (e.g., Ponte and Rosen 2004; Monahan 2006a, 2008). These studies have shown that higher-order moments of the joint surface wind PDF must be known to derive a joint PDF of surface stress. Hence, the question arises of how to account for the deviations from Gaussian distributed winds, especially over the Southern Ocean, where winds regularly violate the Gaussian assumption (Tuller and Brett 1984; Pavia and O'Brien 1986; Simmonds and Dix 1989; Wanninkhof et al. 2002).

With the need for improved seasonal and climate predictions and more available computational power, the spatial and temporal resolution of weather and climate models continues to increase (Delworth et al. 2012; Small et al. 2014; Haarsma et al. 2016; Mizuta et al. 2017). As computational capabilities improve, models explicitly resolve more nonlinear surface processes and enhance the non-Gaussianity of surface variables, such that they have begun to advance beyond the assumption of Gaussian distributed surface variables (Blein et al. 2020, and references therein). Unsurprisingly, atmosphere–ocean interaction and related model biases have been identified as some of the biggest challenges in long-range weather forecast and climate models (White et al. 2017; Huang et al. 2020; Lin et al. 2020). To better represent highly nonlinear fluxes, parameterizations of bulk air–sea fluxes need to account for the non-Gaussianity of variables at high spatial resolution (Wanninkhof 1992; Wanninkhof et al. 2002; Edson et al. 2013).

In this paper, we represent surface wind variability in terms of PDFs to understand its physical drivers on time scales longer than five days. We also use time-varying PDFs to learn about SO surface wind biases and the occurrence of extreme surface stress (>0.4 Pa). First, we derive time-varying PDFs from reanalysis and scatterometer data (section 2a) and then apply a principal component analysis (section 2d) to decompose the PDFs into their leading modes. Second, we show the close relation of the leading modes in zonal wind and stress to the SAM (section 3). Third, we represent the zonal and meridional covariability in the surface wind and stress as the superposition of a few patterns that are driven by changes in the strength or position of extratropical cyclones, their frontal structure, and the seasonal cycle (section 4). Fourth, we show how the leading modes map into the climatological wind differences (section 5) and how surface wind extremes can be understood with respect to these climatological differences (section 6). Although we acknowledge that correlation is not causation, we finish by suggesting how this empirical mode can be linked to nonlinear surface processes and therefore the dynamics that influence SO surface climate (section 7a).

2. Methods

a. *Time-varying PDFs of Southern Ocean wind and stress from ERA5*

The 10-m surface winds (u_{10} and v_{10}) and surface stresses (τ_x and τ_y) from the ERA5 reanalysis (European Centre for Medium-Range Weather Forecasts fifth-generation reanalysis for the global climate and weather; Hersbach et al. 2018a, 2020) between 55° and 63°S (the latitude limits of Drake Passage) are used to derive statistically robust, empirical time-evolving PDFs in the Southern Hemisphere (SH) between 1979 and 2017. The latitude limits are chosen such that the wind patterns and fronts over the ocean are solely driven by extratropical storms, rather than by flow around topography or subtropical

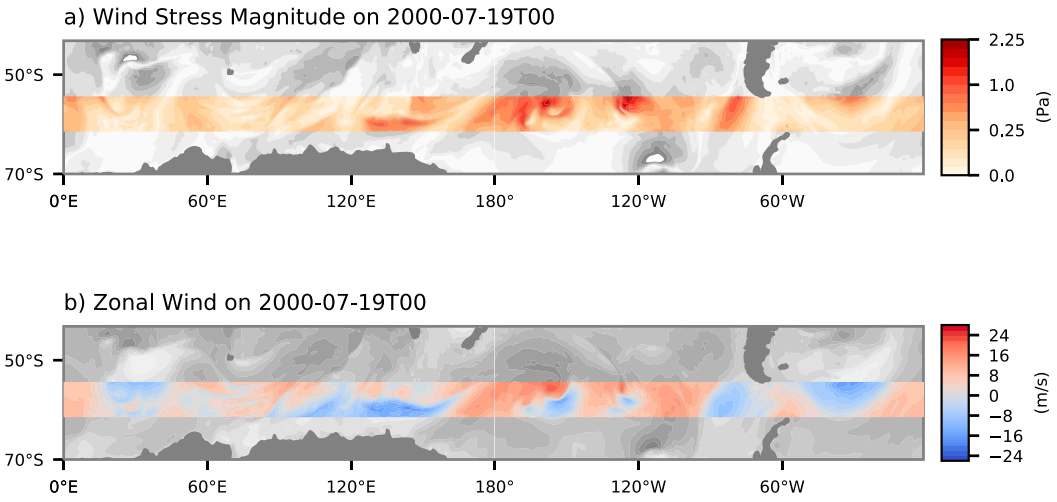

FIG. 1. (a) Surface wind stress magnitude over the Southern Ocean on 19 Jul 2000. Data from the Drake Passage range are in red shading. (b) Zonal surface winds u_{10} for the same date as in (a).

dynamics (Figs. 1a,b). This region also coincides with the areas of most intense and most frequent extratropical storms over the SO (Turner et al. 1996; Hoskins and Hodges 2005; Lim and Simmonds 2007). The same analysis for a broader latitude range leads to similar results, albeit with increased noise levels (appendix A; Gille 2005).

Note that these surface winds differ from zonal-mean zonal winds or even meandering jets (Fig. 1), also indicated by the fact that the surface eddy kinetic energy exceeds the mean surface kinetic energy by about a factor of 2 (Lin et al. 2018, 2020). However, the midlatitude zonal-mean jet and surface wind variability are still related, as detailed in section 7a.

Without any prior averaging, the hourly and 0.25° data are divided into 5-day chunks starting on 1 January each year. (Leap years have a 6-day chunk at the end of February for computational convenience.) Five-day chunks are selected in order to capture the characteristic time scale of baroclinic wave activity (Blackmon 1976; Wallace et al. 1988; Randel and Held 1991). The 5.4×10^6 data points in each block (1440 longitudes $\times$ 31 latitudes $\times$ 120 h) are used to derive joint histograms of winds and stresses in the zonal and meridional directions for every 5-day period between 1979 and 2017 (see the example PDFs in Fig. 2). Histograms of only the zonal or meridional components are derived from the joint histograms by summing in the respective orthogonal direction. All histograms are then represented as probability density functions $D(\mathbf{u}, t)$ or $D(\boldsymbol{\tau}, t)$ by dividing by the bin width and the total number of data points used in the respective 5-day mean.

Figure 3 shows the resulting time-varying PDFs for 5-day increments of zonal wind and stress. For the SO, zonal wind PDFs have a nonzero mean, with a long tail on the negative side of the PDF that can be diagnosed from negative skewness (Fig. 3a). This suggests low-frequency covariability between the distribution's mean and skewness (Monahan 2004). These changes in the 5-day zonal wind PDFs are echoed by similar variability patterns in the zonal stress PDFs (Fig. 3b). Increases in the mean zonal wind are associated with extreme zonal stresses (exceeding the 90th percentile ≈ 0.4 Pa; Fig. 3b, green dashed line), and weak zonal winds coincide with exceptionally weak zonal stress (episodes in September and December in Fig. 3). This covarying behavior of mean and skewness distinguishes the derived PDFs from a Gaussian PDF, a feature that will be further analyzed in sections 3 and 4.

Note that this analysis requires data on short time intervals. ERA5 is one of a few datasets that provides hourly data over the reanalysis period with improved wind statistics compared to ERA-Interim (especially over the SO and along the Antarctic coast; Belmonte Rivas and Stoffelen 2019; Tetzner et al. 2019). Datasets that only provide coarser temporal resolution may miss the dynamics seen in Fig. 3 and likely prohibit possible interpretations of the results.

b. *Time-varying PDFs from CCMPv2 and scatterometer winds*

We also derive surface wind PDFs using three additional Southern Ocean surface wind products. The CCMPv2 (Cross-Calibrated Multi-Platform version 2.0) winds provide 6-hourly fields on a 0.25° grid. The CCMPv2 dataset is derived from ERA-Interim winds blended with all available wind observations to produce a gridded product: observational gaps between scatterometer swaths are filled with winds from ERA-Interim (Wentz et al. 2015). For this study, data points between these swaths are ignored, and CCMPv2 data are used only if they are informed by one or more observation.

In addition to the blended winds, we also analyze two Level 3 (L3) wind products that are based on the Advanced Scatterometer (ASCAT) aboard the European Meteorological Operational Satellites *MetOp-A*, *MetOp-B*, and *MetOp-C*. Remote Sensing Systems (RSS) provides ASCAT winds on a 0.25° grid for ascending and descending swaths. We treat these as quasi-twice-daily observations (Ricciardulli and Wentz 2016). Similarly, Global Ocean L3 *MetOp-A* winds from CMEMS (Copernicus Marine Environment Monitoring Service) are also provided twice daily at 0.25° grid spacing [based on the Royal Netherlands

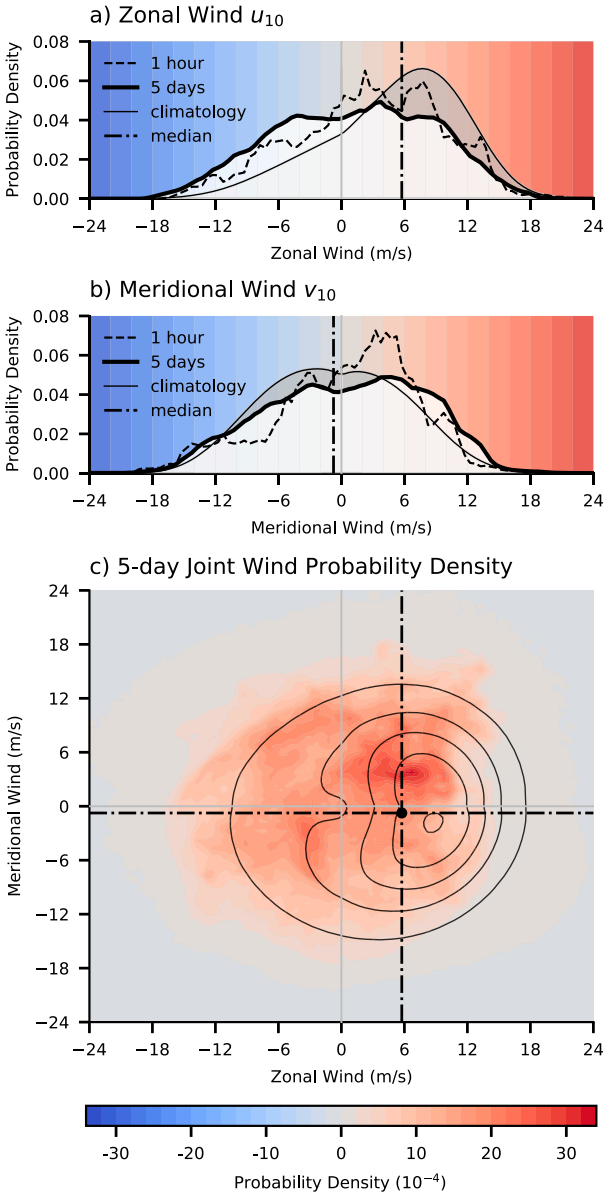

FIG. 2. (a) Zonal wind PDFs for the 1-h time step shown in Fig. 1b (dashed black line), 5-day periods including this time step (thick black line, white shading), and the climatology (thin black line with filled gray area). The background coloring corresponds to the color scale in Fig. 1b. (b) As in (a), but for the meridional wind component. (c) The corresponding joint wind PDFs for a 5-day time step and the climatological joint distribution in black contours in 4×10^{-4} intervals. The black dash-dotted lines indicate the climatological distribution medians.

Meteorological Institute (KNMI); Driesenaar et al. 2019]. Time-evolving PDFs for 5-day bins are derived for the three scatterometer wind products in the same way as for ERA5. CCMPv2, RSS ASCAT, and *MetOp-A* ASCAT each provide 4%–13% as many data points as provided by ERA5, with large seasonal variability due to sea ice cover. (Satellite products have a spatial coverage 50%–85% per 5-day period compared to ERA5; see Fig. B1 in appendix B) Here, RSS ASCAT and *MetOp-A* ASCAT includes data points under rain. Since rain biases are mainly limited to low winds, the results are not expected to be sensitive to them (Driesenaar et al. 2019).

c. *Effective degrees of freedom*

The data from ERA5 and scatterometer products are spatially and temporally correlated, such that their effective degrees of freedom (DOF) are much less than the number of data points used to establish each 5-day distribution. This effect is illustrated in Fig. 2, where we compare ERA5 PDFs derived from a single time step (1 h, dashed black lines), five days (solid black lines), and the climatology (gray shading). We see that the 5-day PDFs are smooth compared to the 1-day PDFs. The effective DOF is calculated by estimating the spatial and temporal decorrelation scales in ERA5 (appendix B). The effective DOF for the zonal wind u_{10} is 175 and for the meridional wind v_{10} 1070. The e-folding scales are 2.4 days and 1100 km in the zonal and 40 km in the meridional direction for u_{10}, and 1.4 days and 130 km in the zonal and 40 km in the meridional direction for v_{10} (Fig. B1). These characteristic scales suggest that we can assume each 5-day PDF to be a robust estimate, which implies that differences between successive PDFs are due to changes in physical drivers, rather than uncertainties in the estimate of the PDF. The 5-day joint PDFs have more noise than their meridional or zonal projections because the same number of effective DOF as in the one-dimensional PDFs is now spread over the squared number of spatial data points (Fig. 2c).

d. *Principal component analysis of time-varying PDFs*

To derive the covariances between the time-varying PDFs, the PDFs of zonal wind $\mathbf{D}(u_{10}, t)$ and stress $\mathbf{D}(\tau_x, t)$ for ERA5, CCMPv2, RSS ASCAT, and *MetOp-A* ASCAT are decomposed into their leading-order modes using singular value decomposition ($\mathbf{D} = \mathbf{U\Sigma E}^{\mathrm{T}}$). The probability variation patterns $\mathbf{E}$ [empirical orthogonal functions (EOFs)] are multiplied by the singular values from $\mathbf{\Sigma}$, so that they have units of probability density. The columns of $\mathbf{U}$ [principal components (PCs)] are unit vectors that specify the time variability of the EOF.

We have decomposed both the one-dimensional PDFs in the zonal and meridional directions, and the joint PDFs. The following analysis primarily focuses on the leading modes in the zonal direction as well as the leading modes from the joint PDFs, because the other decompositions mainly express the same variability (Fig. 4). The cross-correlation between PCs of all decompositions as well as estimates of the nonlinear dependence of the PCs can be found in the online supplemental material.

The first three EOFs of the zonal and meridional wind PDFs are very similar for all four wind products (Fig. 5; higher modes are in the supplemental material), and each EOF explains a similar fraction of the total variance in the respective data products. The fraction of variance explained exceeds a null-hypothesis threshold defined by decomposing Gaussian noise, implying that the EOF has more structure than we would expect to see if the signal were simply Gaussian white noise

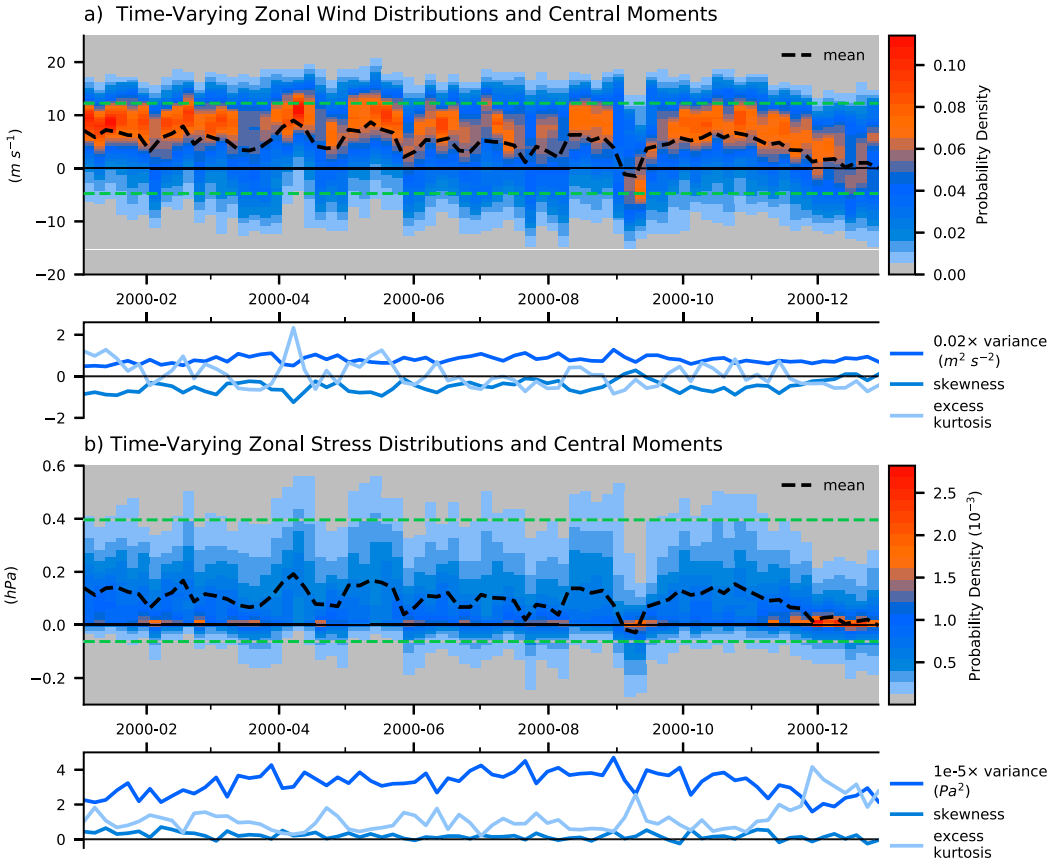

FIG. 3. (a) One year of time-varying zonal wind PDFs. Each pixel indicates the probability of wind occurring in a 0.5 m s^{-1} wind interval within 5 days. The black dashed lines indicate the PDF mean, and the green dashed lines are the 0.1 and 0.9 quantiles of the climatological distribution. The blue lines in the subpanel show the higher moments of the PDF: variance ($m^2 s^{-2}$), skewness (unitless), and excess kurtosis (unitless). The variance is rescaled by a factor of 0.02. (b) As in (a), but for zonal stress. In this case the variance (Pa^2) is rescaled by 10^{-5}.

(Figs. 5g,h; Preisendorfer *N* test, Preisendorfer and Mobley 1988; von Storch and Zwiers 1999, ch. 13).

The first two EOFs of u_{10}^{PDF} and v_{10}^{PDF} are similar to EOF decompositions of an ensemble of parametric Gaussian jets, as computed by Monahan and Fyfe (2006). As in Monahan and Fyfe, we find dipoles and tripoles as leading modes (Figs. 5a–d). This shows that the statistical model outlined by Monahan and Fyfe (2006) for EOFs of varying prescribed Gaussian or arbitrarily shaped distribution functions is akin to a simplified version of the decomposition we perform here. The major difference in our analysis is that while Monahan and Fyfe used a fixed, but arbitrary, shape to mimic the zonal mean zonal jet, here we have no reason to assume a specific shape for the distribution. Instead we seek to find modes of an empirical PDF that capture more degrees of freedom than a predefined, more restricted shape function. As we will describe in detail below, this empirical approach suggests a better interpretation of the results (section 7).

Note that relative to ERA5, the spatial coverage and amount of data vary between the scatterometer wind products from a minimum of 30% for *MetOp-A* ASCAT in austral winter to about 85% in austral summer in CCMPv2, and the effective DOF of the scatterometer wind PDFs is substantially less than for ERA5 (appendix B). Despite the varying effective DOF, the decomposition of all scatterometer wind PDFs appears to be robust, even for the joint PDFs that have a weaker signal-to-noise ratio (Fig. 2c and section 2a). Hence, the analysis in sections 3 and 4 focuses on ERA5 because it provides a complete dataset of surface wind and stress PDFs with the highest signal-to-noise ratio. Equivalent results can also be derived from the scatterometer data, although the climatologies of the scatterometer PDFs differ relative to ERA5, as outlined in section 5.

3. Zonal wind and stress covariability and its relation to SAM

In this section we show that the leading modes of the surface stress PDFs, and therefore the ocean's forcing, are tightly linked to the leading modes in the zonal wind PDFs. For both wind and surface stress, the first two modes explain 90% of the variance, while the PCs of the first and second modes of wind and stress are nearly identical.

Figures 6a and 6b compare the first three EOFs of the zonal wind and zonal stress PDFs from ERA5 with their climatology.

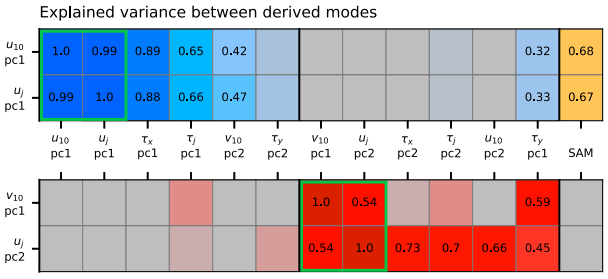

FIG. 4. Squared correlations (explained variances) between leading PCs and the southern annular mode (SAM). Modes in the green boxes are used in sections 3 and 4, namely the first PCs of the u_{10}^{PDF} decomposition (u_{10}^{PDF} PC1), the joint wind PDF decomposition ($\mathbf{u}^{\mathrm{PDF}}$ PC1), the u_{10}^{PDF} decomposition (v_{10}^{PDF} PC1), and the second PC of the joint wind PDF decomposition ($\mathbf{u}^{\mathrm{PDF}}$ PC2). Modes where most of the variance is explained by u_{10}^{PDF} PC1 are marked with blue (upper half) and modes where most of the variance is explained by v_{10}^{PDF} PC1 are in red (lower half). The explained variance shared with SAM is shown in orange in the rightmost column. Only explained variances larger than 0.25 are indicated.

The first zonal wind PDF EOF (u_{10}^{PDF} EOF1; 72% of variance) is asymmetric around the median of the PDF. Positive values of the PC1 time series are associated with less frequent weak zonal winds (around zero) and more frequent zonal wind speeds exceeding 10 m s^{-1} (Fig. 6a, dark blue line). Since the zonal wind PDFs are in general skewed, the range over which the first EOF reduces the zonal wind PDF (from −10 to 5 m s^{-1}) is larger than the range over which the EOF enhances the zonal wind PDFs (5–15 m s^{-1}; Fig. 6a). This asymmetry is even more pronounced in the first EOF of zonal stress PDF [τ_x^{PDF} EOF1 in Fig. 6b, correlation coefficient $r(u_{10}^{\mathrm{PDF}}$ PC1, τ_x^{PDF} PC1) = 0.94]. A positive value of the stress PC1 reduces the stress PDF's peak (positive, but close to zero); it increases the likelihood of extreme eastward stresses (>0.4 Pa; Fig. 6b, green dashed line) but decreases the likelihood of westward stresses. Hence, the leading EOFs can be interpreted as shifting the center of the zonal wind PDF, accompanied by asymmetric flattening of the typically double exponential zonal stress PDF (Gille 2005).

The second EOFs of the zonal wind and stress PDFs are both roughly symmetric around their median (Figs. 6a and 6b, dotted gray lines), indicating fluctuations in wind or stress that might be captured by their variance. This mode shows that increases in the likelihood of winds being concentrated near the PDF's center are accompanied by a roughly symmetric reduction in the likelihood of winds occurring in the tails of the PDF, and vice versa. The PCs of the second EOFs are also well correlated between the wind and wind stress PDFs (correlation coefficient $r = 0.92$; Fig. 6d) but only explain about 18% of the overall variance in probability density. The PCs of the third EOFs explain even less variance in probability density (<5%) and are close to the noise level (section 2d).

Figures 6c and 6d show the PCs of the leading two EOFs in the zonal wind and zonal stress PDF for 15 years. The similarity between the wind and stress PDF PCs suggests that the zonal stress PDF variability can be mostly explained by the zonal wind PDF. The first two PCs of τ_x^{PDF} together explain 92% of the variance and resemble the first two PCs of u_{10}^{PDF}. This is surprising since stress depends not only on zonal winds but also on meridional winds and nonlinear boundary layer processes that are represented through the drag coefficient [Eq. (1)]. Hence, the similarities between u_{10}^{PDF} and τ_x^{PDF} suggest that the zonal wind may dominate the zonal stress variability and/or that the meridional wind and surface drag covary with the zonal wind, as further discussed in sections 4 and 7a. In Figs. 6a and 6b, a shift of the zonal wind PDF maximum by 5 m s^{-1} ($+1u_{10}^{\mathrm{PDF}}$ PC1) leads to a 30% reduction in the likelihood of wind stresses PDF around ±0.1 Pa around the peak and a 50% increase in the likelihood of stresses larger than 0.4 Pa [green dashed line in Fig. 6b; Eq. (1)]. The close relationship between the first PCs of u_{10}^{PDF} and τ_x^{PDF} also appears in their power spectra (Fig. 7a, blue and red line): the leading PCs of the zonal wind PDF and stress are indistinguishable on time scales between 250 days and one month, with a distinct peak at the semiannual cycle. The power on the semiannual scale is well documented for the Southern Hemisphere midlatitudes (Simmonds and Jones 1998; Simmonds 2003) and may be related to the seasonal heat storage of the upper ocean (van Loon 1967).

The first PCs of the wind and stress PDF exhibit strong year-to-year variability. This variability is coherent with the SAM with zero phase lag on all scales between a month and four years except on the seasonal and semiseasonal cycle (Figs. 7b and 7c; the correlation coefficient of u_{10}^{PDF} PC1 and SAM = 0.82). This coherence extends to significant poleward trends in u_{10}^{PDF} PC1 and τ_x^{PDF} PC1 similar to the observed poleward trends for SAM [about 0.054 ± 10^{-5} PC1 per decade, p value = 0.001, in line with Thompson et al. (2000), Thompson and Solomon (2002), and Lin et al. (2018)]. Here, SAM is defined as the leading-order mode of the 5-day-mean zonal-mean zonal wind in the SH extratropics (Thompson and Wallace 2000; Thompson and Woodworth 2013). Hence, long-term trends in the surface stress PDFs are related to trends in the zonal mean wind. The coherence between PC1 and SAM implies a relationship between local wind probabilities (represented by the PDFs) and larger-scale zonal mean winds (represented by SAM). The weaker coherence at the semiannual and annual frequencies is an artifact of the conventional definition of SAM, which removes annual-cycle variability before the SVD decomposition (appendix C).

The second PCs of u_{10}^{PDF} and τ_x^{PDF} show regular seasonal cycles with some noise (Fig. 6d). They also have some power on the semiannual scale (Fig. 7a, dashed blue and dashed red line), which might be related to imperfect reconstruction of the semiannual cycle due to noise and/or the nonlinear dependence on the first mode (see the supplemental material). These seasonal cycles capture variability that is similar to a variance measure (EOF2 in Figs. 6a,b), which implies that the seasonal atmospheric circulation is weaker than its month-to-month or year-to-year variability (Trenberth 1991). In other words, in the latitude band of the Drake Passage, the seasonal cycle is responsible for symmetric changes in the zonal wind PDF more than asymmetric shifts in the distribution's center and tails.

Note that, by construction, the EOFs of the PDFs are uncorrelated but not independent. Even though the leading EOFs are an orthogonal, linear independent basis, they can still covary in a more complex fashion. Indeed, the scatter of

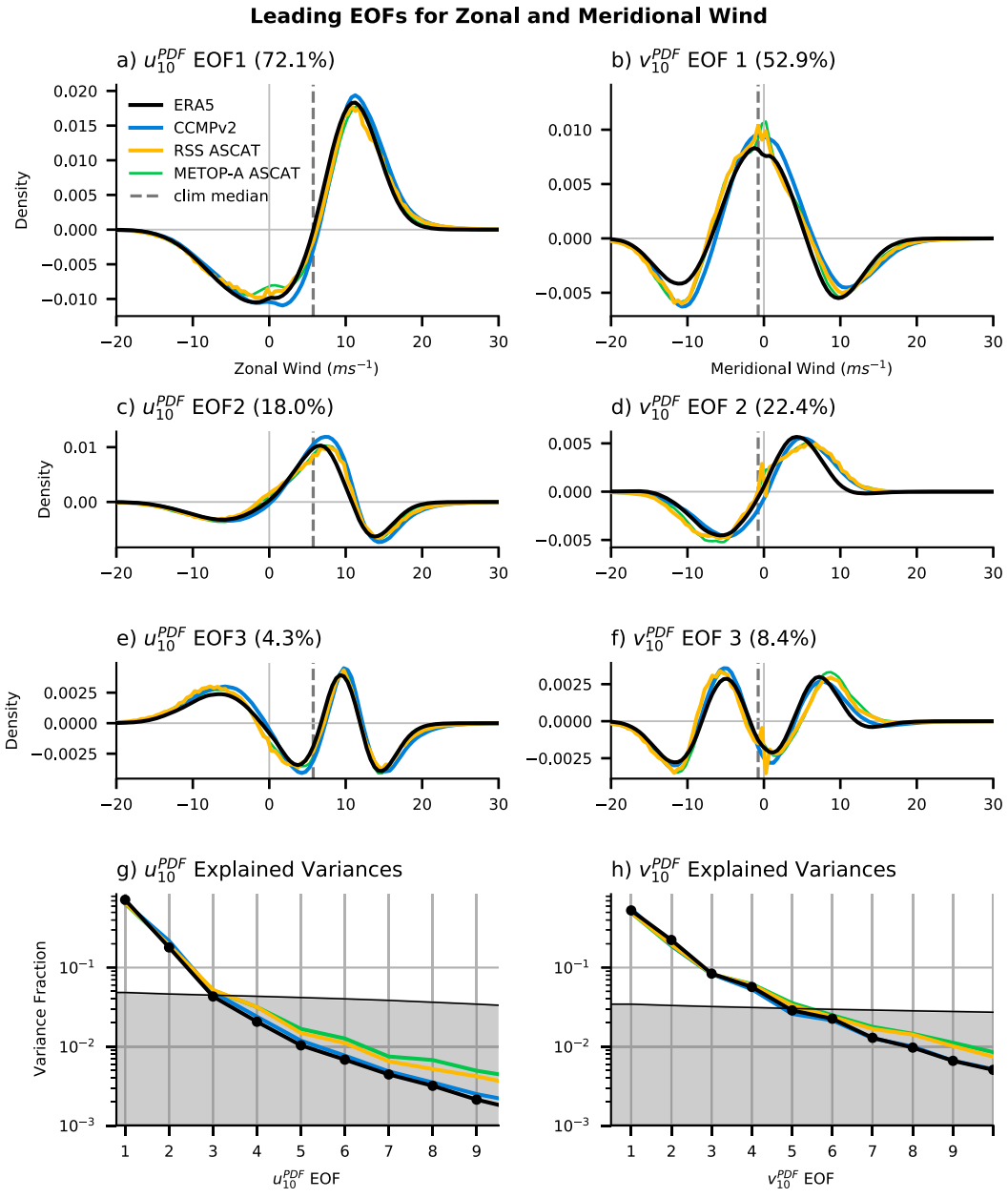

FIG. 5. First three leading EOFs of (a),(c),(e) zonal and (b),(d),(f) meridional wind for ERA5 (black), CCMPv2 (blue), RSS ASCAT (orange), and *MetOp-A* ASCAT (green) with their fraction of explained variance in the title. Explained variance for the first 10 modes in log-scale for the (g) zonal wind and (h) meridional wind PDFs. Gray shading indicates the fraction of variance explained by a decomposition of Gaussian noise (Preisendorfer *N* test).

the first and second zonal wind PDF PCs indicate that very strong, or very weak events of PC1 are more likely during a negative PC2; that is, extreme zonal stresses are more frequent during short events in austral winter (March–October) and less frequent in austral summer (December and January; see the supplemental material). This shows that the derived basis set is neither completely independent nor necessarily unique, and that there are some richer dynamics on the seasonal scale that are not explored at this point (Fig. 7a). Nevertheless, we show in the following sections 5 and 6 that even the linear, empirical decomposition used here is useful for simplifying and elucidating the leading-order dynamics.

4. Synoptic variability in the joint wind and stress PDF decompositions

In this section, we extend the analysis of the zonal wind and stress PDF covariability to include the meridional component. This allows us to represent a significant fraction of variance with a small number of functions, which also reveals the

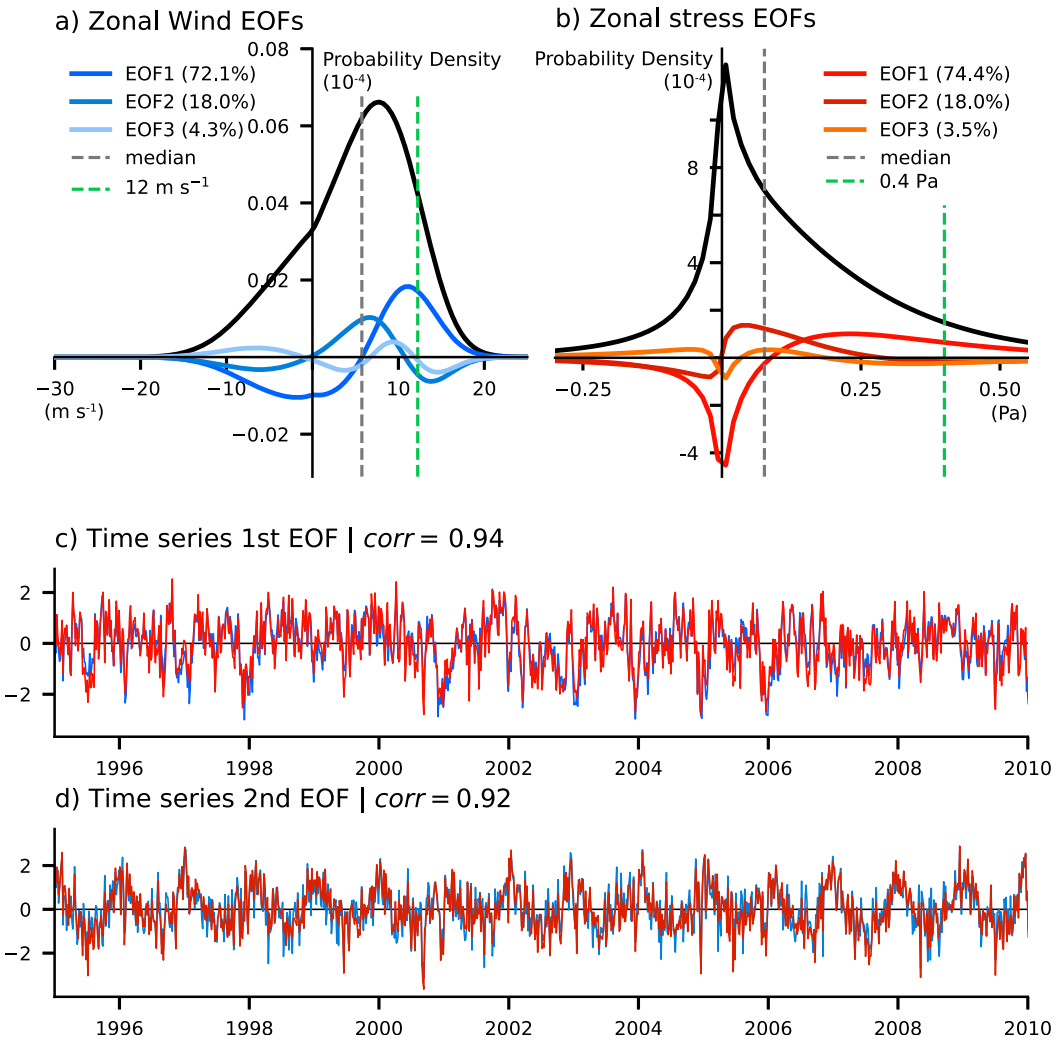

FIG. 6. Leading EOFs for (a) zonal wind and (b) stress. The climatology is indicated in black, the median with dashed gray lines, and the 0.9 quantiles (12 m s^{-1} and 0.4 Pa) as green dashed lines. The EOFs' explained variances are indicated in the legend. (c) PCs of the first mode of zonal wind (u_{10}^{PDF} PC1; blue) and the first mode of zonal stress (τ_x^{PDF} PC1; red). Their respective correlations are given in the panel headings. (d) As in (c), but for the second mode (u_{10}^{PDF} PC2 and τ_x^{PDF} PC2).

synoptic-scale drivers of the variance. Figure 8 shows the first two EOFs of the joint surface wind ($\mathbf{u}^{PDF}$ EOF1 and $\mathbf{u}^{PDF}$ EOF2 in Figs 8c,d) and the joint surface stress ($\boldsymbol{\tau}^{PDF}$ EOF1 and $\boldsymbol{\tau}^{PDF}$ EOF2 in Figs 8f,g), as well as the projected means in the meridional and zonal directions (Figs 8a,b,e,h,i,j). The first two modes of the joint surface wind PDF show the same patterns as the one-dimensional decomposition, but they explain less variance (together 58% of the total variance). A smaller fraction of explained variance is not surprising since the joint decompositions have to represent the variance for the square of the number of grid points compared to the one-dimensional decomposition.

The first joint wind mode ($\mathbf{u}^{PDF}$ EOF1; 41% variance explained) includes the variability of the u_{10}^{PDF} EOF1 and v_{10}^{PDF} EOF2 [$r(\mathbf{u}^{PDF}$ PC1, u_{10}^{PDF} PC1) = 0.99, $r(\mathbf{u}^{PDF}$ PC1, v_{10}^{PDF} PC2) = 0.68], which implies that u_{10}^{PDF} PC1 and v_{10}^{PDF} PC2 are also correlated [$r(u_{10}^{PDF}$ PC1, v_{10}^{PDF} PC2) = 0.65]. The zonal and meridional means show the same patterns as the related one-dimensional decompositions. The similarity of the patterns and the shared variance between the zonal and meridional modes suggests that there is a shared variability that shifts the joint PDF mainly in the zonal direction. This variability is well described by SAM [$r(\mathbf{u}^{PDF}$ PC1, SAM) = 0.82].

In addition to enhancing eastward zonal winds, this SAM mode of the joint PDF EOF corresponds to a poleward shift of the PDF's maximum (similar to v_{10}^{PDF} EOF2; cf. Figs. 8a and 5a, and Figs. 8e and 5d). This covariability of both wind components is a consequence of the structure and variability of extratropical cyclones. Since the joint PDFs are a reduced representation of the maps of surface winds (Fig. 1), their shape and variability also reflect the synoptic variability of surface wind or, similarly, sea level pressure. The joint PDF measures the intensity of the cyclone fronts, as well as of the

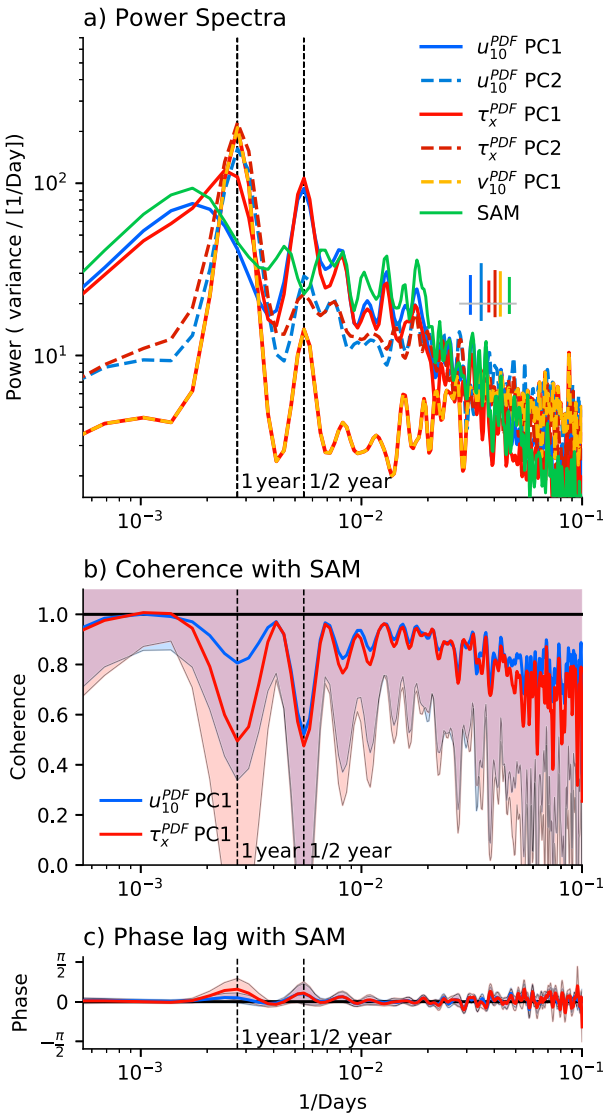

FIG. 7. (a) Power spectra of u_{10}^{PDF} PC1 (blue), u_{10}^{PDF} PC2 (dashed blue), τ_x^{PDF} PC1 (red), τ_x^{PDF} PC2 (dashed dark red), v_{10}^{PDF} PC1 (orange-red dashed), and SAM (green). The uncertainty is indicated as the 95th percentile range by the inlaid bar plot on the right in (a). (b) Coherence of u_{10}^{PDF} PC1 (blue) and τ_x^{PDF} PC1 (red) with SAM as defined in appendix C. (c) Coherence phase of u_{10}^{PDF} PC1 and τ_x^{PDF} PC1 with SAM. Shadings in (b) and (c) indicate ± 1 standard deviation of the estimated coherence or phase respectively (Bendat and Piersol 2010). Power spectra and cospectra are estimated using a Welch's overlapping segment method with a segment length of 8 years (584 data points) with a Hanning window on the detrended data. The resulting lines are smoothed with a Lanczos filter of 2×10^{-3} days^{-1} window length.

cyclones themselves in the latitudes of Drake Passage (Hoskins and Bretherton 1972, and subsequent studies). This is possible because extratropical storms are inherently asymmetric, and their dynamics are linked to their frontal systems (Shapiro and Keyser 1990; Neiman and Shapiro 1993; Simmonds et al. 2012; Schemm and Wernli 2014).

The cyclones' imprint on the surface wind PDFs is characterized by intensified winds in the cyclones' cold sectors that shift the PDF maximum toward more frequent strong westerlies (Fig. 9a, horizontal red arrows). The stronger westerlies are accompanied by intense, but narrow southward flow ahead of the cold front (low-level jet; Fig. 9a, curved red arrow). These cold-front winds add the southward inclination of the dipole pattern of the joint PDF (Fig. 8c, green dot). The surface winds on both sides of the cold front imprint on the first EOFs for both wind and stress PDFs. While the joint wind PDF's maximum shifts along a diagonal through the PDF's median (Fig. 8c black dot), the joint wind stress PDF weakens at the peak and is enhanced mainly in the southeastward direction (Figs. 8f and 8g, orange and green dots, note the nonlinear color scale). At times when the first PC is positive, the EOFs indicate less equatorward flow and less weak zonal wind regimes, as they typically appear in the wake of an eastward propagating storm (gray arrows in Fig. 9a correspond to orange dot in Fig. 8c).

The leading mode of the joint PDF can be understood as a measure of the cyclone activity in the latitude limits of Drake Passage. The cyclone activity is highly coherent with SAM (Fig. 7b blue line; power spectra of $\mathbf{u}^{\mathrm{PDF}}$ PC1 and u_{10}^{PDF} PC1 are indistinguishable; see the supplemental material). A positive SAM is associated with stronger fronts (Fig. 9a; Rudeva and Simmonds 2015), projects onto the leading mode of the joint wind PDF and the joint stress PDF, and enhances extreme eastward stresses [$>$0.4 Pa; Fig. 8f (note the nonlinear color scale); corr($\mathbf{u}^{\mathrm{PDF}}$ PC1, $\boldsymbol{\tau}^{\mathrm{PDF}}$ PC1) = 0.81]. By contrast, a negative SAM leads to weaker fronts and enhanced equatorward flow and stresses (Fig. 9b, blue arrows). Since the latitude limits of the Drake Passage capture the southward barotropic shift of the tropospheric zonal mean zonal winds, the leading wind PDF mode can be interpreted as either a shift of the storm track around its climatological position (Lorenz and Hartmann 2001) or a change in wind intensity (Shaw et al. 2016, 2018).

The second joint wind mode has a more circular structure and captures changes in the width of the joint PDF (Fig. 8, explained variance 16%). The projections of the $\mathbf{u}^{\mathrm{PDF}}$ EOF2 on the zonal and meridional axes are similar to the u_{10}^{PDF} EOF2 and v_{10}^{PDF} EOF1 [Figs. 5b,c; $r(\mathbf{u}^{\mathrm{PDF}}$ PC2, u_{10}^{PDF} PC2) = 0.73, $r(\mathbf{u}^{\mathrm{PDF}}$ PC2, v_{10}^{PDF} PC1) = 0.81], although they contain variance due to processes other than storm intensity driven by SAM.

The second mode of the joint wind PDF also leads to a dipole in the joint stress PDF [$r(\boldsymbol{\tau}^{\mathrm{PDF}}$ PC2, $\mathbf{u}^{\mathrm{PDF}}$ PC2) = 0.84]. The dipole structure arises because the second joint wind EOF is not precisely symmetric. Nevertheless, the second joint stress mode is mostly confined around the origin (within $\pm$0.2 Pa), which illustrates again how changes similar to the wind's variance are not solely responsible for extreme surface stresses. Higher-order modes are not judged to be statistically different from what we would expect to find by computing EOFs of Gaussian noise and are not explored here (Fig. 10; Monahan and Fyfe 2006).

5. Differences in reanalysis and scatterometer products

The leading-order modes of the surface wind PDFs provide a framework for interpreting differences between surface wind

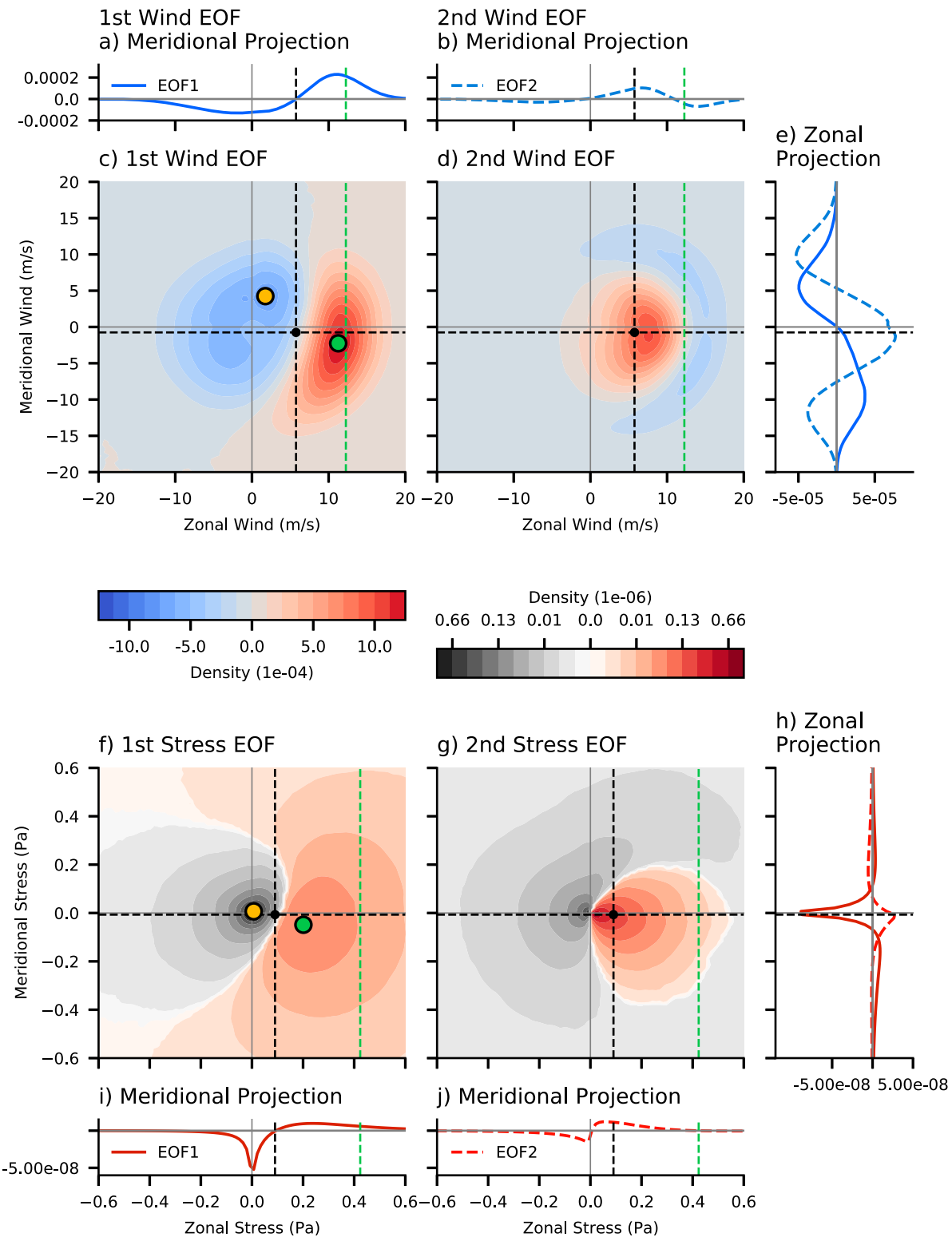

FIG. 8. (a),(b) Meridional mean of the first (blue) and second (blue dashed) joint wind EOFs. Also shown are the first two EOFs of the joint PDFs of (c),(d) wind and (f),(g) stress and their projections, as well as (e) the zonal mean of the first and second joint wind EOFs, (h) the zonal mean of the first (red) and second (red dashed) joint stress EOFs, and (i),(j) the meridional mean of the first and second joint stress EOFs, respectively. The orange and green dots in (c) and (f) indicate the maximum and minimum of the respective EOF. The shading for stress modes is adjusted following a $(\cdot)^{1/4}$ scale.

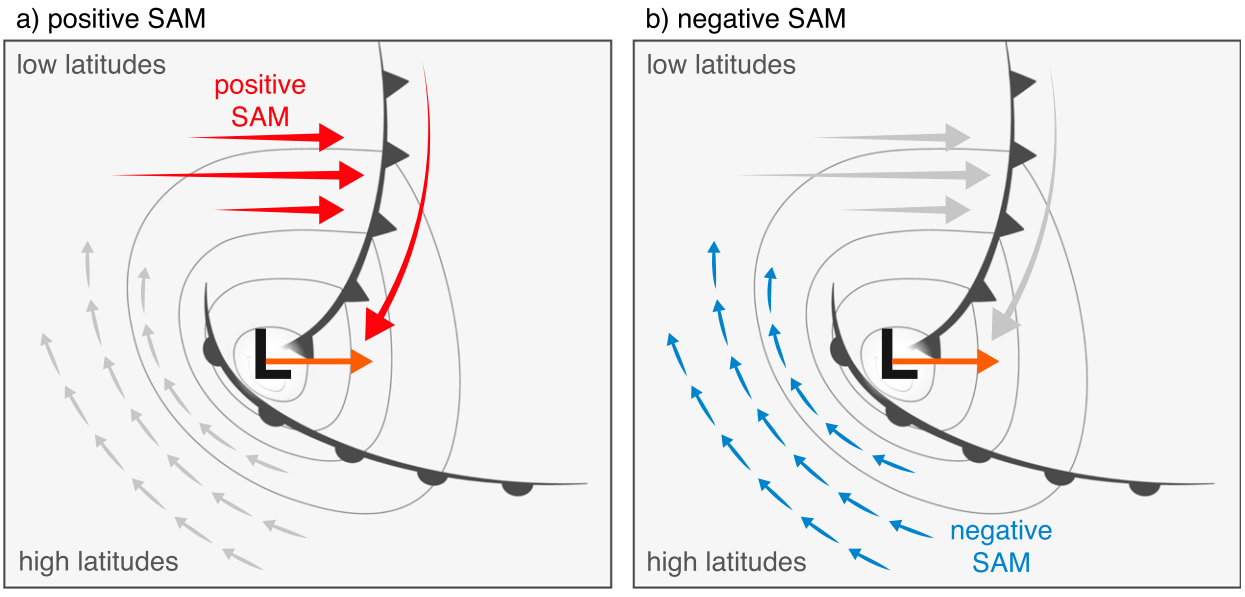

FIG. 9. Schematic of surface winds in the moving frame of an extratropical cyclone in the SH for (a) positive and (b) negative SAM inferred from Shapiro and Keyser (1990), Neiman and Shapiro (1993), Bengtsson et al. (2009), Catto (2018), and Sinclair et al. (2020). In (a) strong westerly winds behind the cold front and alongfront winds ahead of the cold front (in red) are enhanced during positive SAM phase. In (b) southeasterly winds not associated with the cold front (in blue) are enhanced during negative SAM. Light gray lines show idealized sea level pressure lines, and the orange arrow indicates the average travel direction of the cyclone.

products. Figure 11 shows climatologies of meridional and zonal wind PDFs derived from ERA5 (1979–2017), CCMPv2 (1978–2017), RSS ASCAT (2007–16), and *MetOp-A* ASCAT (2007–16). The log-scaling exposes velocity differences of up to 30% at a given probability density level (for $|u| > 20\,\mathrm{m\,s^{-1}}$; Figs. 11a,b). Alternatively, this is expressed as a probability density change for a given velocity compared to ERA5 (Figs. 11c,d). While ERA5 and *MetOp-A* ASCAT have narrower tails that rarely exceed $30\,\mathrm{m\,s^{-1}}$ in the zonal direction and $25\,\mathrm{m\,s^{-1}}$ in the meridional direction, CCMPv2 and RSS ASCAT assign probability densities of 10^{-7} to velocities up to $40\,\mathrm{m\,s^{-1}}$ in the zonal direction and $33\,\mathrm{m\,s^{-1}}$ in the meridional direction. (In the Drake Passage latitude band, a probability density level of 10^{-7} corresponds to an area of about $2\,\mathrm{km^2}$ having a particular wind value at any given time.) That is, compared with ERA5, CCMPv2 and RSS ASCAT have eastward or westward wind speeds that exceed $25\,\mathrm{m\,s^{-1}}$ about 30–100 times more often (Figs. 11c,d).

Differences near the PDF centers fall into two simple patterns that approximately match the leading EOFs for the u_{10}^{PDF} and v_{10}^{PDF} PDFs (cf. Figs. 11e,f with Figs. 5a,b). Here we show the difference of *MetOp-A* ASCAT, CCMPv2, and RSS ASCAT from ERA5 to emphasize these anomaly patterns. For the zonal wind, the three scatterometer products have PDFs that are higher around $10\,\mathrm{m\,s^{-1}}$ and lower around zero compared to ERA5. Since the node point of this dipole sits at the median of the ERA5 PDF (Fig. 11e, dashed gray line), this pattern is associated with shifts in the maxima of the PDFs (section 3) and leads to differences in the PDF means, medians, and standard deviations (Fig. 12a).

A different behavior appears in the meridional direction (Figs. 11b,d,f). The scatterometer PDFs show a symmetric difference relative to ERA5 and CCMPv2, with fewer winds around zero and more winds at about $\pm 10\,\mathrm{m\,s^{-1}}$. This widening of the PDF implies a difference in variance (section 3). However, these differences are not well captured by the variance metric because differences in the center may be partly

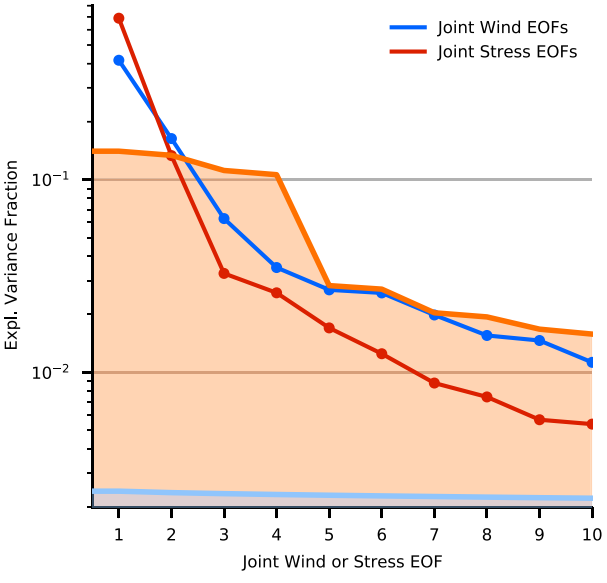

FIG. 10. Explained variances for the joint wind PDF (in blue) and the joint stress PDF (in red) on a log scale. The orange and light blue lines show the 95% levels for the joint stress and wind estimated from the Preisendorfer and Mobley (1988) *N* test after 1000 repetitions.

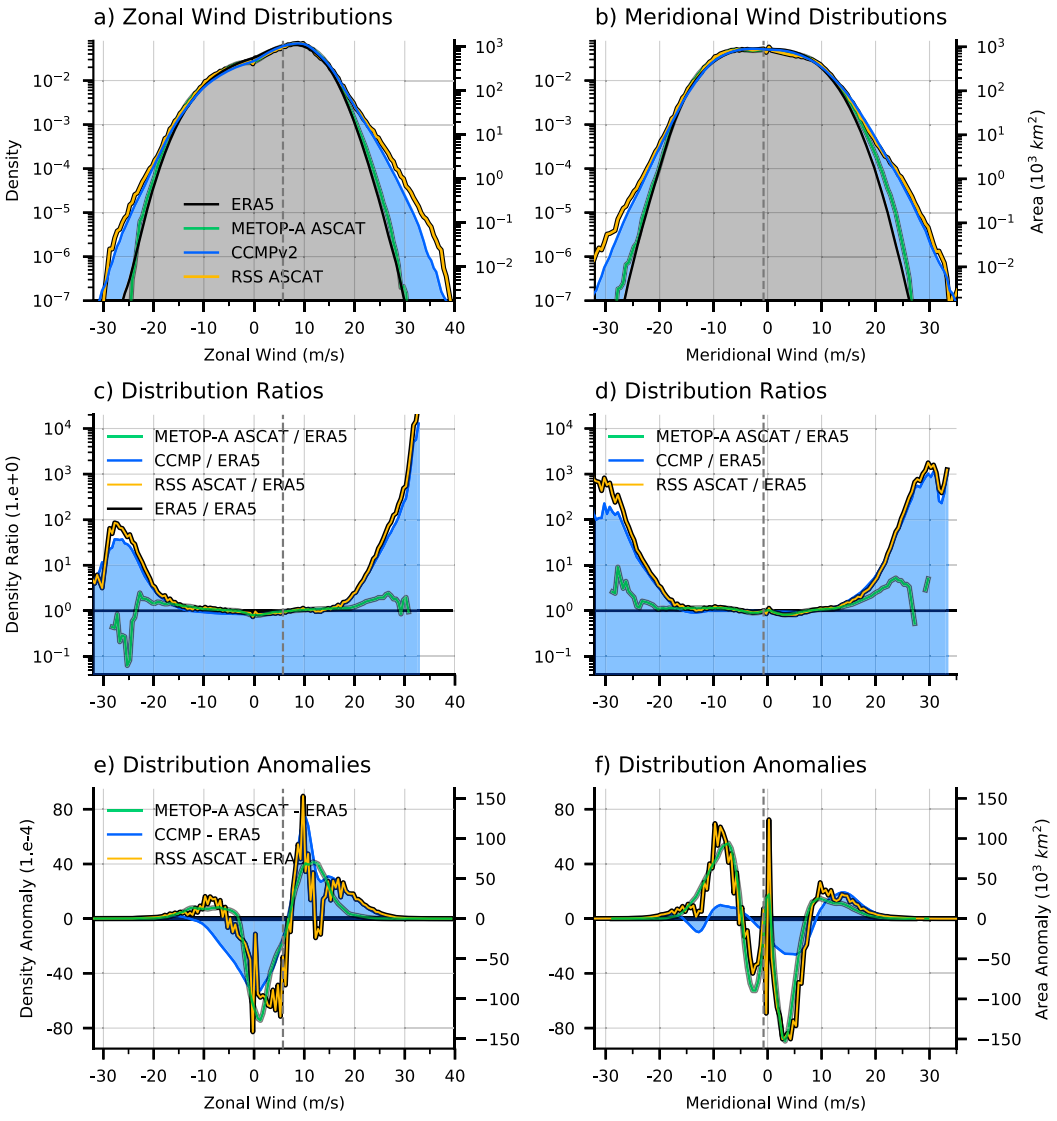

FIG. 11. PDFs of (a) zonal and (b) meridional wind between 55° and 63°S derived from ERA5 reanalysis (black), observationally constrained CCMPv2 winds (blue line and shading), *MetOp-A* ASCAT (green), and RSS ASCAT scatterometer winds (orange) with log scaling. The scaling on the right ordinate is the area equivalent for a given probability density in 10^3 km^2. (c),(d) As in (a) and (b), but shown as ratios compared to the ERA5 PDF. (e),(f) As in (a) and (b), but shown as differences from the ERA5 PDF for zonal and meridional wind, respectively.

compensated by differences in the tails such that changes in variances are rather small (Fig. 12b dashed lines). As an alternative to the metrics provided by mean and variance, the climatological bias pattern in Fig. 11f is better understood as resembling the v_{10}^{PDF} PC1 (Fig. 5b). This approach works well for both ASCAT products but less well for CCMPv2 (Fig. 11f). The spikes around zero in RSS and *MetOp-A* ASCAT are likely due to low-wind rain biases in the wind retrieval algorithm (Driesenaar et al. 2019).

This analysis shows that differences between scatterometer-based products and model-based winds (ERA5) are systematic, and resemble the signatures of SAM-related wind variability (sections 3 and 4). Moreover, these results imply that estimates of SO winds can be improved by combining observed winds with constraints from larger-scale dynamics.

6. Leading modes of the most extreme winds

Informed by the differences between PDFs for different wind products, we can now investigate the leading modes for the most extreme values in the u_{10}^{PDF} and v_{10}^{PDF} wind PDFs. (Most extreme refers here to $|u_{10}|$ or $|v_{10}|$ exceeding 20 m s^{-1}.) Analyzing the frequency of the most extreme winds allows us to understand the occurrence of extreme energy fluxes into the ocean surface ($\propto u_{10}^3$). Figure 13 shows the leading zonal and meridional PDF EOFs as in Fig. 5, but now added to their

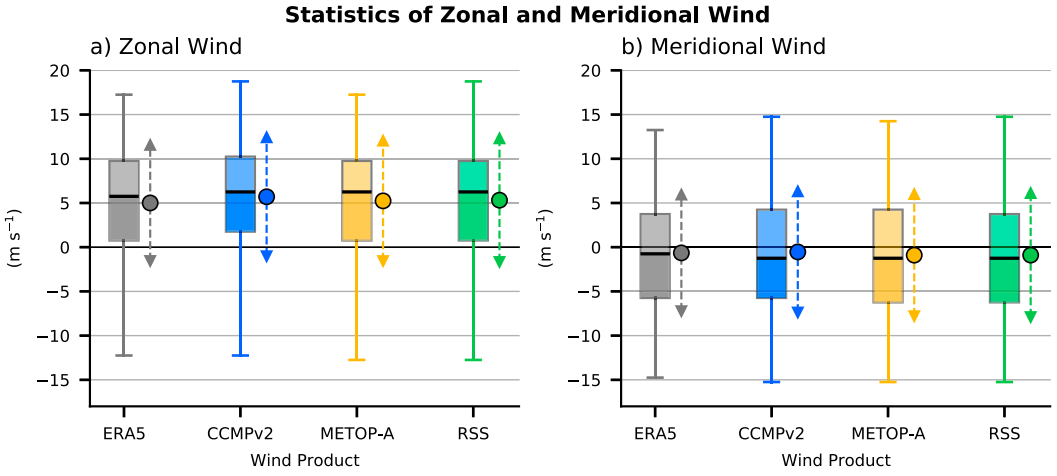

FIG. 12. (a) Zonal wind and (b) meridional wind statistics in the Drake Passage limits as box-and-whisker plots for ERA5 (gray), CCMPv2 (blue), *MetOp-A* ASCAT (orange), and RSS ASCAT (green). The boxes indicate the limits of the first and third quartiles surrounding the medians (horizontal black lines), and the whiskers indicate the 1% and 99% quantiles. The colored dots are the mean centered between the range of ±1 standard deviation (dashed lines between triangles).

respective climatology (gray shading for ERA5 and *MetOp-A* ASCAT; blue shading for CCMPv2 and RSS ASCAT). To emphasize the changes in the PDF tails, in Figs. 13a and 13b we show only values outside $\pm 20\,\mathrm{m\,s^{-1}}$ on a log scale. In this scaling, anomalies relative to the climatology are not area-equivalent, and negative deviations appear larger than positive deviations.

The first u_{10}^{PDF} EOF extends to the most extreme wind conditions. An increase in u_{10}^{PDF} PC1 corresponds to a shift in the u_{10}^{PDF} EOF1 maximum, which covaries with an increase in the extreme zonal winds (cf. Figs. 6a and 13a). This correlation is generally stronger for ASCAT-based wind products than for ERA5 or CCMPv2, such that an increase in PC1 by one standard deviation means a doubling in the likelihood of the most extreme wind velocities in the first EOF from RSS ASCAT, but less in other products (Fig. 13a).

The first v_{10}^{PDF} EOF is less consistent between the four chosen wind products compared to u_{10}^{PDF} EOF1. A typical narrowing of the v_{10}^{PDF} PDF leads to a reduction by a factor of 3–5 in the occurrence of velocities in the tails (Figs. 5b and 13b). Changes in extreme winds associated with the second and higher EOFs are even less coherent, and are not further analyzed here.

We note that here the SVD decomposes the covariances of very different scales and must be treated with caution. The SVD is an axis rotation along the most common mode of variability in the covariance matrix and these axes (EOFs) are mainly defined by fluctuations in the PDF centers $[O(10^{-2})]$, while small fluctuations in the tails $[O(10^{-6})]$ only marginally contribute to the modes of the covariance matrix.

To test the robustness of the modal decomposition, we rederive the SVD for the log-PDFs $\log[D(u, t)]$. Use of the log enhances the variability of the tail compared to fluctuations in the center. The overall shape of the leading-order modes remains robust under a log-weighting for all wind products but with less explained variance for the first modes (supplemental material). The enhancement of the most extreme winds in the u_{10} PDF EOF1, as observed in Fig. 13, also remains robust, while changes in the v_{10} PDF EOF1 are not.

7. Discussion

a. *Large-scale circulation establishes surface winds and stress PDFs*

As we showed in section 3, the time evolution of the first two modes of both the one-dimensional and joint surface wind PDFs resembles that of the leading modes in surface stress PDF (Figs. 4 and 6). These two modes trace changes in the conversion of excess atmospheric angular momentum to surface

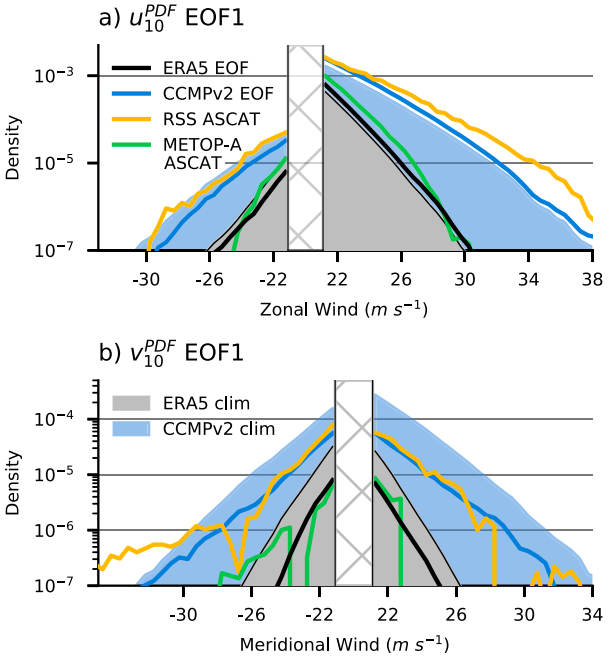

FIG. 13. First EOFs of the (a) zonal and (b) meridional wind added to their climatology and shown on a log scale. Data between $\pm 21\,\mathrm{m\,s^{-1}}$ are masked out to emphasize the variability in the tails.

momentum fluxes, without explicitly resolving the cascade of processes involved in converting atmospheric momentum to stress.

The first mode is mainly a positional shift of the zonal wind PDF maximum that leads to more frequent extreme zonal stresses (>0.4 Pa; Figs. 6a,b) accompanied by changes in the PDF's shape. Southern Ocean zonal surface winds are negatively skewed and limited in their extremes (>12 m s^{-1}) due to their nonlinear relation with surface drag [Eq. (1)]; we showed that a shift in the PDF maximum does not imply a proportional increase in the PDF's extreme quantile (Figs. 3 and 6a). Instead, the higher-order dependence of surface stress on wind leads to changes in the mean, skewness, and kurtosis; this is captured in the first EOF (PC1 u_{10}^{PDF} and PC1 $\boldsymbol{\tau}^{\mathrm{PDF}}$ in Fig. 14). Changes in the variance, however, are mainly captured in the second EOF (PC2 u_{10}^{PDF} in Fig. 14).

The EOF decomposition of the time-varying joint PDFs adds a meridional component to predominantly zonal wind and stress variability. As the zonal wind PDF maximum increases in the leading-order mode, the meridional component shifts southward (Figs. 8c,e). This joint mode is highly coherent with SAM as a measure of the zonal-mean zonal wind in the free troposphere (Thompson and Woodworth 2013; Thompson and Barnes 2014).

Our analysis indicates some relation between the dynamics that establish SAM and perturbations of the (mainly zonal) wind statistics. We hypothesize that the changes in the shapes of the PDFs are the reason why the first mode EOFs can be related to dynamical drivers, as we outline below. This is potentially one of the few examples where EOF decompositions of the variance align well with a dynamical interpretation (section 3).

Dynamical links are not required to create patterns like the $\mathbf{u}^{\mathrm{PDF}}$ or $\boldsymbol{\tau}^{\mathrm{PDF}}$ EOF1s, but in this case the patterns result from links across several dynamical scales. One could design a two-dimensional shape function that accounts for deviations of a joint wind PDF from a two-dimensional Gaussian as it changes its mean zonal wind (Thompson et al. 1983; Monahan and Fyfe 2006, 2009). By requiring that the mean meridional winds as well as the zonal skewness and kurtosis correlate with the mean zonal wind (section 2d; Fig. 14), one would obtain a modeled PDF with a shape that changes systematically with perturbations of the mean zonal wind. A decomposition of a perturbation ensemble of this modeled joint PDF (section 2a) would then return a dipole patterns that could look like Figs. 8c and 8d. This statistical exercise would mimic some of the physical constraints that stem from the nonlinearities in the atmospheric boundary layer (ABL). While the statistics of synoptic-scale eddies (i.e., storms) alter the mean wind components, asymmetric PDF shapes result from the perturbations of the ABL by the mean and the synoptic scale (Monahan 2006a). Hence, SAM can be interpreted as an integrator of synoptic-scale ABL perturbations that results in characteristic wind and stress distribution changes in the tails of the distribution.

In our analysis we find the PDF's covariability with SAM to be intrinsic for the empirically derived modes. This is

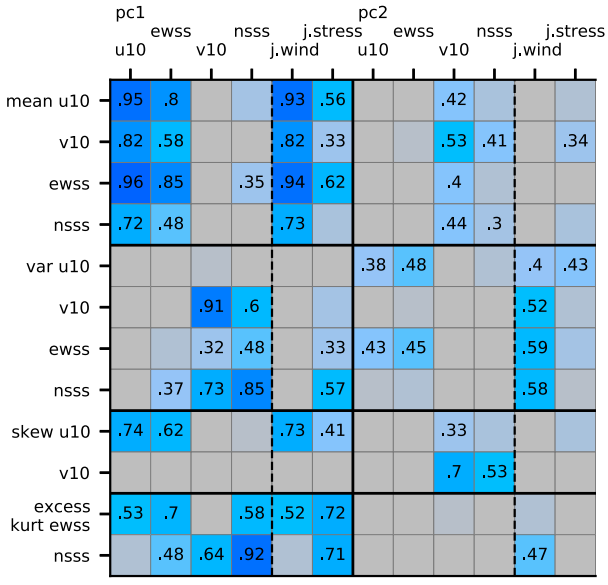

FIG. 14. Explained variances between PCs from the SVDs of directional wind and stress and first four moments of the PDF. Explained variances are shown for measures of zonal surface wind (u_{10}), meridional surface wind (v_{10}), east–west stresses (ewss), and north–south stresses (nsss).

interesting, because SAM is a proxy for the eddy-momentum flux convergence in midlatitudes (Karoly 1990; Feldstein and Lee 1998; Hartmann and Lo 1998; Limpasuvan and Hartmann 2000; Lorenz and Hartmann 2001) and hypothesized to be altered with climate change [as summarized in Screen et al. (2018)]. This would suggest that the interaction between eddy activity and the surface establishes the leading mode of the joint stress PDF (section 4). In this context we suggest that SAM is better viewed as a tracer for intensity of fronts and/or latitudinal shifts in the storm activity, rather than changes in the zonal mean surface winds (Lorenz and Hartmann 2001; Fig. 8) because this storm activity dominates the surface wind distribution over the SO (Fig. 9; Lin et al. 2018). Hence, we think we can go beyond a statistical interpretation of the empirical modes. Based on our observations, we outline in the following paragraphs how the observed leading joint PDF EOFs are consistent with dynamics that are linked to the transformed Eulerian mean (TEM) circulation (Andrews and McIntyre 1976, 1978; Edmon et al. 1980), part of which are captured by SAM (section 3, section 4, and Fig. 7).

While SAM describes the variability of upper-level wave breaking via angular momentum flux convergence in the midlatitudes, surface stress under extratropical cyclones is the dominant mechanism to remove this excess angular momentum from these latitudes (section 3; Lorenz 1967; Peixoto and Oort 1992; Hartmann and Lo 1998; Schneider 2006). These dynamics can be related to the zonal surface stress PDF as follows. In the absence of mountain torque, the steady state, vertically integrated zonal mean zonal momentum balance in midlatitudes can be written to leading order as

$$\partial_y \int_0^\infty \widetilde{[u^*v^*]}\, dz = [\tilde{F}], \tag{2}$$

where $[u^*v^*]$ is the zonal-mean eddy-momentum flux in the atmosphere, $[F]$ is the zonal mean surface drag, and $\widetilde{(\cdot)}$ indicates the average over a 5-day interval [see, e.g., chapter 11 of Peixoto and Oort (1992); Edmon et al. 1980]. We assume a steady state, since the contribution of the tendency in the zonal mean momentum balance is small on time scales longer than the characteristic time scales of single eddies in the upper troposphere (cf. Gerber and Vallis 2007; Simpson et al. 2013). We neglect mountain torque because we analyze only the latitude band of Drake Passage where no continents are present. Equation (2) illustrates that the zonal-mean zonal surface drag in the latitude limits of Drake Passage is the result of the vertically integrated atmospheric zonal momentum balance, and, as we showed in section 3, the zonal mean surface drag in each 5-day interval can be written as

$$[\tilde{F}] \simeq \overline{\tau}_x + \mathrm{PC1}_{\tau_x}(t) \sum_{i=-\infty}^{\infty} \tau_x(i)\, \mathrm{EOF1}_{\tau_x}(i)\, \Delta\tau_x, \tag{3}$$

where $\overline{\tau}_x$ is the climatological zonal surface stress and $\tau_x(i)$ is the surface stress for bin-index i of the PDF. In the limit of small $\Delta\tau_x$ this implies that

$$\partial_y \int_0^\infty \widetilde{[u^*v^*]}\, dz \simeq \overline{\tau}_x + \mathrm{PC1}_{\tau_x}(t) \int_{-\infty}^{\infty} \tau_x\, \mathrm{EOF1}_{\tau_x}\, d\tau_x. \tag{4}$$

Equation (4) describes how the vertical integral of the momentum-flux convergence in midlatitudes is balanced by the climatological eastward stress and its first EOF. The long-term mean eddy momentum flux convergence is represented by the offset of the zonal wind and stress mean ($\overline{u}_{10}$ or $\overline{\tau}_x$) away from zero, while its short-term variability is mainly balanced by adjusting the amplitude and sign of the first EOF of the zonal surface stress PDF (Figs. 6a,b). Note that, since net eddy momentum flux convergence is the result of irreversible Rossby wave breaking in the upper troposphere (Vallis 2006, ch. 12); Ait-Chaalal and Schneider 2014; Lutsko et al. 2017; Schneider 2006, and references therein] it imposes a causal relation between wave activity aloft and surface stress distribution changes on time scales of about 5 days. One may be able to describe this suggested relation in a more exact version of Eq. (4), which would describe a closed balance between atmospheric angular momentum and empirical modes of the zonal surface stress PDFs, similar to a stochastic differential equation that could be used to explain the evolution of the PDF (Risken 1996). In addition, τ in Eq. (4) depends on C_d in Eq. (1), which indicates the critical role of C_d in shaping the surface wind and stress PDF (Fairall et al. 2003; Monahan 2006a, 2008), as well as the relation of the eddy-driven jet to surface drag (Mbengue and Woollings 2019).

The approximate short-term zonal-mean balance [Eq. (4)] also suggests a hypothesis for the origin of the observed dipole structure in $\mathbf{u}^{\mathrm{PDF}}$ and $\boldsymbol{\tau}^{\mathrm{PDF}}$EOF1. While the off-zero center of the joint distribution (Figs. 8c,f, black dot and Fig. 2c, black contours) again represents the climatological balance of surface drag against upper-level eddy momentum flux convergence, the dipole in the EOF1 patterns is a signature of variability that one would expect from synoptic adjustment processes of the TEM circulation. By sampling in 5-day increments, we have sufficient temporal resolution to distinguish adjustments that seem to perturb the meridional overturning circulation, including its Eulerian part, the "Ferrell cell" (Vallis 2006, ch. 11.7). The wind and stress EOFs vary in response to perturbations of the eddy momentum flux convergence aloft that are partly balanced by meridional flow near the surface ("downward control"; Haynes et al. 1991). It means that anomalously strong momentum flux convergence (i.e., positive SAM) is partly balanced by equatorward flow, which in turn leads to poleward (southward) flow near the surface to conserve mass. This anomalous poleward Coriolis acceleration in the boundary layer leads to anomalous zonal surface winds and stresses (Figs. 8c,f, green dots; Peixoto and Oort 1992, ch. 11; Limpasuvan and Hartmann 2000). Hence, it is plausible that the observed dipole structures of the leading joint PDF modes are created by the superposition of the vertically integrated balance suggested in Eq. (4) and dynamic adjustments that are needed to maintain this balance. While the processes described here are still at the hypothesis stage, we suggest that idealized model studies should be able to elucidate the role of large-scale adjustment processes on surface stress statistics.

At the surface, this strong coherence between SAM and the leading modes also reveals how SAM relates to extreme winds within synoptic-scale systems (Claud et al. 2009; Booth et al. 2010). A positive SAM increases the probability of wind patterns that are associated with fronts under storms (Fig. 9a, red arrows; Rudeva and Simmonds 2015). Extreme zonal winds and stresses behind the cold front and stronger southward stress ahead of the cold front lead to the southeastward shift of the maximum in $\mathbf{u}^{\mathrm{PDF}}$ EOF1 and $\boldsymbol{\tau}^{\mathrm{PDF}}$ EOF1 (Figs. 6a,b and 8c,f). In turn, a negative SAM is associated with fewer extreme westerly winds (or even no predominant westerly winds) and instead enhanced equatorward winds and stresses from the southwest. This SAM mode can be attributed either to shifts of the cyclone centers (storm tracks) into or out of Drake Passage latitudes (Lorenz and Hartmann 2001) or to changes in their intensity (Shaw et al. 2016, 2018). Either mechanism alters the wind and stress PDFs, with an EOF pattern that also extends to the tails of the PDF (section 6; Sampe and Xie 2007; Lin et al. 2018).

The second mode of variability is by construction linearly independent of the first mode, but there are higher-order dependencies (see the supplemental material). The second mode describes symmetric contraction and widening of the PDF that can be captured by a change of the variance, with small changes in the mean (Figs. 5b, 6, and 14). This mode explains about 18% of the zonal and 53% of the meridional wind variability, mainly due to changes on annual and semiannual time scales (Figs. 7a and 14). It is symmetric and concentrated around the PDF's center with little or no influence on extreme winds and only mild impact on extreme stresses (Figs. 8d,g).

b. *Implications for the SO eddy activity*

We have shown that SAM variability and trends represent more complex changes of the atmospheric forcing than just changes in the mean winds and stresses. This provides a new

perspective on the observed increase of eddy activity in the SO that is accompanied by only weak changes in the SO zonal transport (''eddy saturation''; e.g., Hallberg and Gnanadesikan 2006; Meredith and Hogg 2006; Böning et al. 2008). While changes in the mean zonal wind stress (i.e., a trend in SAM) may change the larger-scale SO baroclinicity and subsequent mesoscale eddy activity (Thompson and Solomon 2002; Meredith et al. 2012), sections 3 and 6 show that trends in SAM also have a significant impact on extreme stress statistics. Extreme localized wind stress under storms (sections 4 and 7c) can imply stronger wind stress curls leading to localized strengthened Ekman pumping (e.g., O'Neill et al. 2003, 2005; Schneider 2020), which then interact with the mesoscale eddy field. In addition, extreme winds under storms also enhance near-inertial oscillations in the upper ocean (Pollard 1980; Thomson and Huggett 1981; Gill 1984; D'Asaro et al. 1995) and can possibly provide energy for the mesoscale eddy field (Xie and Vanneste 2015; Asselin and Young 2020). Hence, we speculate that a positive SAM trend could increase upper-ocean mesoscale activity by increasing wind extremes, in addition to increasing the mean wind speed and subsequent balances of the larger-scale baroclinicity.

c. *Interpreting the leading-order mode as a dominant mode of SO atmosphere–ocean interaction*

The empirical decomposition of surface wind and stress into two leading modes leads us to ask which mode is responsible for strong air–sea fluxes of energy, momentum, freshwater, and gas associated with SO mixed layer ventilation events (Schulz et al. 2012; Ogle et al. 2018; Tamsitt et al. 2020) and marine cold-air outbreaks (Bracegirdle and Kolstad 2010; Papritz et al. 2015; Fletcher et al. 2016). While SO mixed layer ventilation is observed to be driven by extreme turbulent heat fluxes that often coincide with equatorward winds advecting cold air from the south (Ogawa and Spengler 2019; Bharti et al. 2019; Tamsitt et al. 2020; Song 2020; Song et al. 2020), the same process, described as a marine cold-air outbreak, leads to atmospheric boundary layer deepening (Grossman and Betts 1990; Brümmer 1996; Renfrew and Moore 1999) and affects the synoptic-scale circulation (Papritz and Pfahl 2016). The other possibility of anomalous mixed layer deepening due to purely mechanical forcing from strong zonal winds is unlikely because turbulent kinetic energy fluxes alone are less effective at mixing a stratified boundary layer (Alford 2020). In addition, zonal winds are also likely less effective in maintaining the surface temperature gradients needed for large buoyancy fluxes (Ogle et al. 2018; Tamsitt et al. 2020).

Equatorward winds occur during a negative SAM mode (Figs. 8c,e and 5d) and also during a negative second mode ($\propto$ increasing variance; Figs. 8d,e and 5b), while both modes show some higher-order dependence (supplemental material). Both modes, or their superposition, could capture events that create strong air–sea fluxes associated with mixed layer ventilation and marine cold-air outbreaks. While this second mode has a dominant seasonal cycle, as observed in the mixed layer ventilation (dashed orange-red line in Fig. 7; Tamsitt et al. 2020), SAM explains 67% of the wind variance (Fig. 4) and 33% of the stress variance (not shown).

We suggest that SO mixed layer ventilation is a result of the superposition of SAM and oceanographic preconditions such that enhanced equatorward winds during negative SAM are likely to be conducive to increased turbulent heat fluxes by winter cold air advection (section 4; Fig. 9b). This mechanism is plausible even when taking into account observed long-term trends of SO ventilation and heat content (Gille 2008; Sallée et al. 2010), SAM-like variations in SO mixed layer depths (Cerovečki et al. 2019; Meijers et al. 2019), and the long-term trend to a more positive SAM with more westerly wind extremes in the Drake Passage latitudes (Thompson et al. 2000; Thompson and Solomon 2002; Lin et al. 2018). Because mixed layer ventilation relies on additional limiting factors like seasonal changes in the meridional surface temperature gradient, local insolation, and mixed layer stratification, it is likely that the northward advection of cold polar air during negative SAM modes is more effective in winter when thermodynamic preconditioning favors mixed layer ventilation. This is in agreement with observed mixed layer ventilation and marine cold-air outbreak events that occur preferentially in austral winter (Papritz et al. 2015; Fletcher et al. 2016; Tamsitt et al. 2020): even if SAM exhibits weak seasonality (Fig. 7a) and a small, long-term trend to more positive values, its negative phase is likely the important contributor to trends in highly nonlinear atmosphere–ocean interactions. We hypothesize that exceptionally strong westerly winds (positive SAM) are not enough to drive deep mixed layer ventilation, because they are not the only factor in determining ocean ventilation and they are also not observed as the dominant mechanism perturbing the atmospheric boundary layer.

Even though we do not explicitly analyze atmosphere–ocean heat fluxes in this study, the oceanic and atmospheric processes outlined above suggest that equatorward winds are important for the evolution of both boundary layers and for the exchange of heat and CO_2. As suggested above, upper tropospheric wave breaking controls the statistics of equatorward surface winds, but it can only control the statistics of intensified atmosphere–ocean fluxes if the ocean stratification is responsive to the atmospheric forcing.

d. *Dynamic drivers of climatological differences*

The leading modes of zonal and meridional winds resemble the climatological differences between ERA5, CCMPv2, RSS ASCAT, and *MetOp-A* ASCAT (section 5). These differences also extend to the PDFs' most extreme values (Fig. 11; Gille 2005). The probability of velocities larger than $\pm 20\,\mathrm{m\,s^{-1}}$ is about 100 times higher for CCMPv2 and RSS ASCAT than for ERA5 and *MetOp-A* ASCAT.

These climatological differences also appear in the most extreme values of the leading EOFs (section 6). We found more extreme wind events during positive SAM in RSS ASCAT products than in ERA5 or *MetOp-A* ASCAT products. However, SVD results from the PDF tails must be treated with caution because a distribution's tail is the least certain portion of a PDF given the rarity of these most extreme events, and the covariance is largely determined by the PDF's center (section 6 and appendix B).

These results agree with central-moment-based validations of reanalysis surface winds (Monahan 2006a) in which ERA5 winds show systematic differences compared to ASCAT and wave-

buoy observations (Belmonte Rivas and Stoffelen 2019; Yagi and Kutsuwada 2020). Additionally, the analysis in section 5 hints at reasons why reanalysis surface winds differ (Taboada et al. 2019; Wen et al. 2019; McDonald and Cairns 2020): since differences in surface wind PDFs resemble the leading mode of atmospheric angular-momentum flux convergence (section 7a), they might arise, whether from reanalyses or scatterometers, from errors in the parameterization of boundary layer turbulence or wind retrieval algorithms, errors in representing mesoscale processes associated with cold fronts (Blein et al. 2020), or large-scale biases in the reanalysis momentum budget (Pithan et al. 2016).

The high correlation of the large-scale flow and interproduct surface wind differences can potentially improve surface wind products and subsequently surface wave models (Durrant et al. 2014; Wentz et al. 2015; Ribal and Young 2020; Trindade et al. 2020; Allen et al. 2020). Spectral wave models rely on accurate surface winds and are particularly sensitive to surface wind extremes (Cavaleri 1994; Cardone et al. 1996; Ponce and Ocampo-Torres 1998; Feng et al. 2006; Durrant et al. 2013; Stopa and Cheung 2014; Janssen and Bidlot 2018; Osinski and Radtke 2020). Due to the differences described above and deficits in the momentum balance of atmospheric general circulation models (Pithan et al. 2016), wave hindcast models are commonly tuned to wave buoy observations by adjusting high surface wind speeds. This practice cannot be applied in ''free-running'' surface wave models as part of coupled climate models (Li et al. 2016; Bourassa et al. 2019) because biases in the model mean state of other model components hinder direct validation with in situ observations. At the same time, including surface wave models in a coupled model framework might improve estimates of C_d, which plays a critical role in shaping the surface stress PDF (section 7a; Edson et al. 2013) as well as the large-scale atmospheric flow (Mbengue and Woollings 2019).

8. Conclusions

Southern Ocean surface winds play an important role in ventilating the upper ocean, mainly through short, extreme events of atmosphere–ocean interaction. This study has investigated a statistical representation of surface wind and stress PDFs that connects large-scale modes of atmospheric variability with short-term processes at the atmosphere–ocean interface.

We have derived leading modes of variability of PDFs of surface winds and stresses between 55° and 63°S using four wind products (ERA5, CCMPv2, RSS ASCAT, *MetOp-A* ASCAT). After calculating time-varying PDFs from all available data points in longitude and latitude in 5-day chunks, we use an SVD of the zonal, meridional, or joint PDF. The first two modes of the zonal or meridional wind together explain 90%–92% of the total variance, while the first three modes of the joint wind SVD explain about 65% of the total variance. These decompositions are robust between the wind products, despite differences in their degrees of freedom (section 2d and appendix B).

The first two PCs of the surface stress PDFs explain an equivalent or greater fraction of variance than the first two PCs of the wind PDFs (Figs. 6 and 10), and the temporal variability of the leading wind stress modes (PC1 and PC2) is nearly identical (section 3). This surprising covariability occurs despite the different noise levels in their SVDs (Fig. 6), and may appear because the joint stress PDFs are functionally related to the joint surface wind PDFs [Eq. (1); Monahan 2008].

We would like to put the result in the broader context of atmosphere–ocean coupling:

- PDFs, used in place of mean quantities, are a cornerstone of stochastic climate modeling (Hasselmann 1976). Here we have expanded on this idea, but, instead of creating PDFs for large ensembles (Kay et al. 2015; Maher et al. 2019; Deser et al. 2020; Reimann and von Storch 2020), we have assumed that the governing processes are ergodic in the latitudes of Drake Passage and over short time periods. This has allowed us to derive a time-evolving PDF from a single realization of the winds (here ERA5 reanalysis or direct scatterometer winds). The leading-order variability of the wind PDFs can then be analyzed using an SVD and compared to other models or wind-products. We choose a standard SVD in order to reduce the complexity of the PDF variability to a set of linearly independent lower-dimensional EOFs, although other forms of modal decomposition might be similarly illuminating. One might imagine that analyses that do not constrain orthogonality (rotated EOFs) or incorporate oscillatory behavior (like POPs) would be better for identifying dynamical drivers of the PDF. However, we have shown that even the leading modes of standard EOFs of surface wind and stress PDFs can be related to the leading-order terms of the zonal momentum balance modes [Eq. (4)]. EOFs are an efficient way of capturing larger-scale modes of atmospheric variability (SAM) in surface fields.
- We suggest that the leading modes of decomposed PDFs are dynamically linked to larger-scale drivers. We point out that these links are imperfect because EOF analysis can in general not reconstruct isolated degrees of freedom of a system (Monahan and Fyfe 2006). EOFs of any kind always decompose the variability to a linear basis set that cannot align with the dynamic drivers of a nonlinear system as in this analysis (Figs. S4a,b in the online supplemental material). In addition, the time-varying PDFs themselves are already a reduced representation of the variability, while their decompositions are generic and can be approximated by derivatives of their shape. Given these simplifications, it is interesting that the dynamics that close the zonal momentum balance can apparently be explained by the leading PDF modes (section 7a).
- We showed that only using the first two moments as a basis for air–sea flux estimates is insufficient [also shown by Monahan (2008)]. This assumption is usually made when wind speed is modeled as a Weibull distribution, which can be estimated from independent Gaussian distributions in u and v, with a nonzero mean wind (Hennessey 1977; Justus et al. 1978; Monahan 2007). Deviations from the Weibull distribution can be captured by higher-order moments (Monahan 2006b), but their relations require many degrees of freedom to be well constrained. The SVD of time-varying PDFs used here needs fewer degrees of freedom per time interval to constrain the PDF tails (Fig. 13 and section 2c), and the superposition of a few modes explains most of the time variation of the PDF.

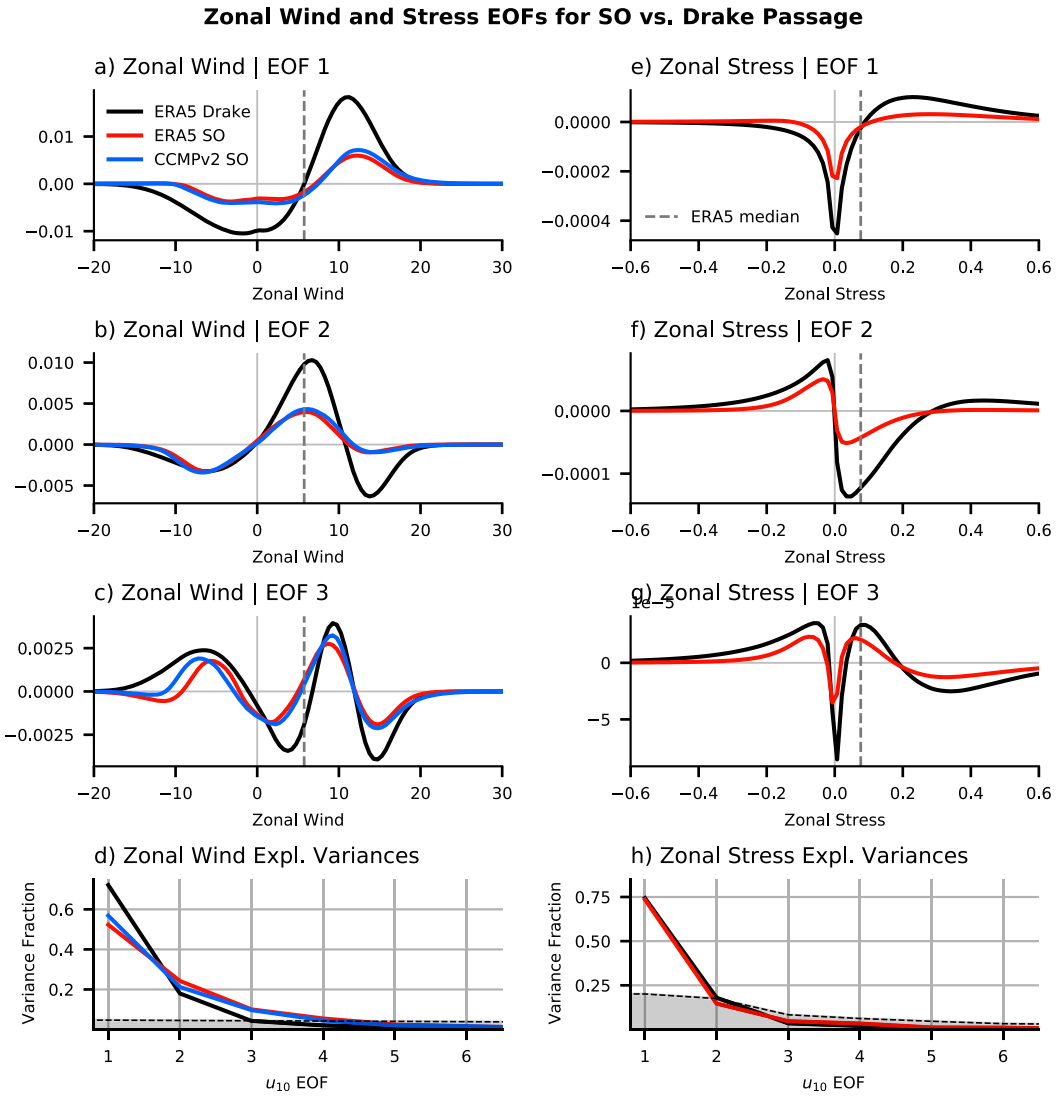

FIG. A1. Leading three EOFs of zonal surface (a)–(c) wind and (e)–(g) stress derived from data in the latitude range of Drake Passage (55°S and 63°S) using ERA5 (black) and for the SO (25°S and 65°S, red for ERA5 and blue for CCMPv2). (d),(h) Explained variances for surface wind and stress with the significance levels derived as in Fig. 5.

- SVDs of surface wind PDFs connect scales of upper-level Rossby wave breaking [SAM, $O(10^6)$ m] with surface winds on the $O(10^4)$ m scales resolved by scatterometer retrievals. This means that scatterometer observations over the SO can be directly related to the large-scale flow of the atmospheric interior [similar to the two-layer model shown in George et al. (2019)]. In addition to validating cyclone intensities in general circulation models and reanalyses, scatterometer winds provide an independent constraint on the atmospheric angular momentum balance on short time scales.
- SVDs of the surface stress PDFs often show a higher signal-to-noise ratio (S/N) than surface winds because they have a steeper decay in the eigenvalues (e.g., Fig. 10). Given that the leading modes of wind and stress capture the same underlying process, the S/N in the commonly analyzed surface winds is likely weaker than in surface stress because of their square relationship [Eq. (1)]. Since scatterometers observe surface capillary waves, which are more closely related to surface stress than to surface winds, we would expect that capillary wave roughness has an even higher S/N than found in this analysis. The initial S/N from capillary wave roughness is reduced when converting to 10-m winds, and only partly recovered again when 10-m winds are converted to stress, due to assumptions about the lower 10 m of the atmosphere, surface waves, and temporal or spatial averaging.

We demonstrated that retaining the full PDFs of variables, rather than reducing them to the moments of the PDF, can be a

useful tool to understand the physical processes likely to govern wind variability. This approach is especially relevant when observing variables near the surface because they are often the result of nonlinear processes that create non-Gaussian distributions. Any kind of spatial or temporal averaging will tend to change fluctuations in the PDF tails. Depending on the averaging scale, the resulting PDFs can be more Gaussian-like, or even more skewed (Proistosescu et al. 2016; Monahan 2018). Even the hourly, 0.25° wind and stress data used here are an approximation to the PDF that would arise from instantaneous point observations. The time and spatial scales that would be required for a sufficient PDF are related to the scales at which momentum is transferred to the ocean. This scale is described by the adjustment time scale of the equilibrium range of the surface wave spectrum (Phillips 1985).

Acknowledgments. MCH and STG were supported by the NASA Ocean Vector Winds Science Team (NASA award 80NSSC19K0059). BDC and STG also received support from the NASA Surface Water and Ocean Topography Science Team (NASA awards NNX16AH67G and 80NSSC20K1136). This study forms a portion of the Ph.D. dissertation of MCH. We thank Adam Monahan and two anonymous reviewers for their thoughtful reviews that have helped to improve this study.

Data availability statement. Data were generated using Copernicus Climate Change Service Information (Hersbach et al. 2018a,b). This study has been conducted using E.U. Copernicus Marine Service Information (accessed 2019). CCMP version-2.0 vector wind analyses are produced by Remote Sensing Systems. Data are available at www.remss.com. C-2015 ASCAT data are produced by Remote Sensing Systems and sponsored by the NASA Ocean Vector Winds Science Team. Data are available at www.remss.com.

APPENDIX A

Analysis of the Larger SO

To test the robustness of the Drake Passage PDFs, the joint PDFs of surface wind and stress are rederived for 25°–65°S to cover the larger SO. Figure A1 compares the EOFs derived for the latitudes of Drake Passage (55°–63°S; black) with EOFs from the SO (red). The figure also shows the EOF decomposition for CCMPv2 winds for the larger SO latitude range.

The first PCs for the larger SO 5-day records explain less variance than do PCs for the Drake Passage latitude band, but the leading-order EOFs have the same shapes in both cases (Fig. A1). A higher noise level and hence less explained variance leads to weaker EOF amplitudes that are less well separated (Fig. A1d). The PCs of the leading modes derived for the SO correlate well with the PCs of the leading modes derived for Drake Passage when the SVDs are performed in one direction only (Fig. A2). The joint PDFs correlate less well, due to the different noise levels and more subtropical wind regimes and/or coastal winds in the large SO case. The larger SO includes additional processes that result in more Gaussian-like primary modes (Fig. A2, right panels).

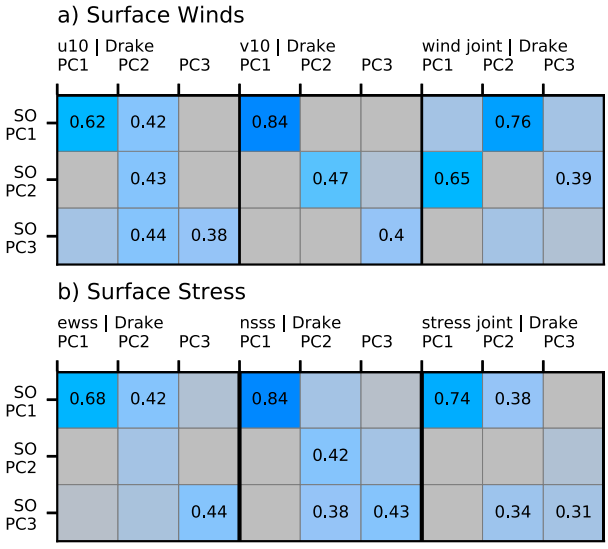

FIG. A2. Correlation of the three leading modes of the zonal u_{10}^{PDF}, meridional v_{10}^{PDF}, and joint wind $\mathbf{u}^{\mathrm{PDF}}$ decompositions from Drake Passage PDFs with the corresponding leading three modes from larger SO PDFs. (b) As in (a), but for zonal τ_x^{PDF}, meridional τ_y^{PDF}, and joint wind $\boldsymbol{\tau}^{\mathrm{PDF}}$.

APPENDIX B

Effective Sample Size

The effective sample size is estimated by calculating the *e*-folding scales in longitude, latitude, and time for the zonal and meridional winds in the latitudes of the Drake Passage (55°–63°S). The ERA5 data are provided on an hourly 0.25° grid such that the autocorrelation function ρ_{dim} in the zonal and time directions can be robustly estimated using a fast Fourier transform. In the meridional direction, we use lagged autocorrelation (Figs. B1a–c). After deriving ρ_{dim} for u_{10}^{PDF} and v_{10}^{PDF} separately in all three dimensions, the effective number of degrees of freedom N_{eff} is calculated by correcting the number of grid points per 5-day period $N = 5\,356\,800$ with

$$N_{\mathrm{eff}} = N\,\gamma(\rho_{u_{10}})\gamma(\rho_{v_{10}})\gamma(\rho_{\mathrm{time}}), \tag{B1}$$

with

$$\gamma(\rho_{\mathrm{dim}}) = \frac{N}{1 + 2\,\mathrm{median}\left[\sum_{1}^{n-1}\left(1 - \frac{k}{n}\right)\rho_{\mathrm{dim}}(k)\right]}, \tag{B2}$$

where k is the lag of the autocorrelation function (von Storch and Zwiers 1999, ch. 6). We take the median of the PDF of all possible autocorrelation lengths n to have an estimate that is less dependent on the truncation of ρ_{dim}.

The number of data points differs between the products because the spatial coverage and time steps differ. To calculate N_{eff} for CCMPv2, RSS ASCAT, and *MetOp-A* ASCAT, we adjust N and $\rho_{\mathrm{time}}(k)$. The autocorrelation ρ_{time} is adjusted by a factor of 1/6 for the 6-hourly CCMPv2 data and by a factor of

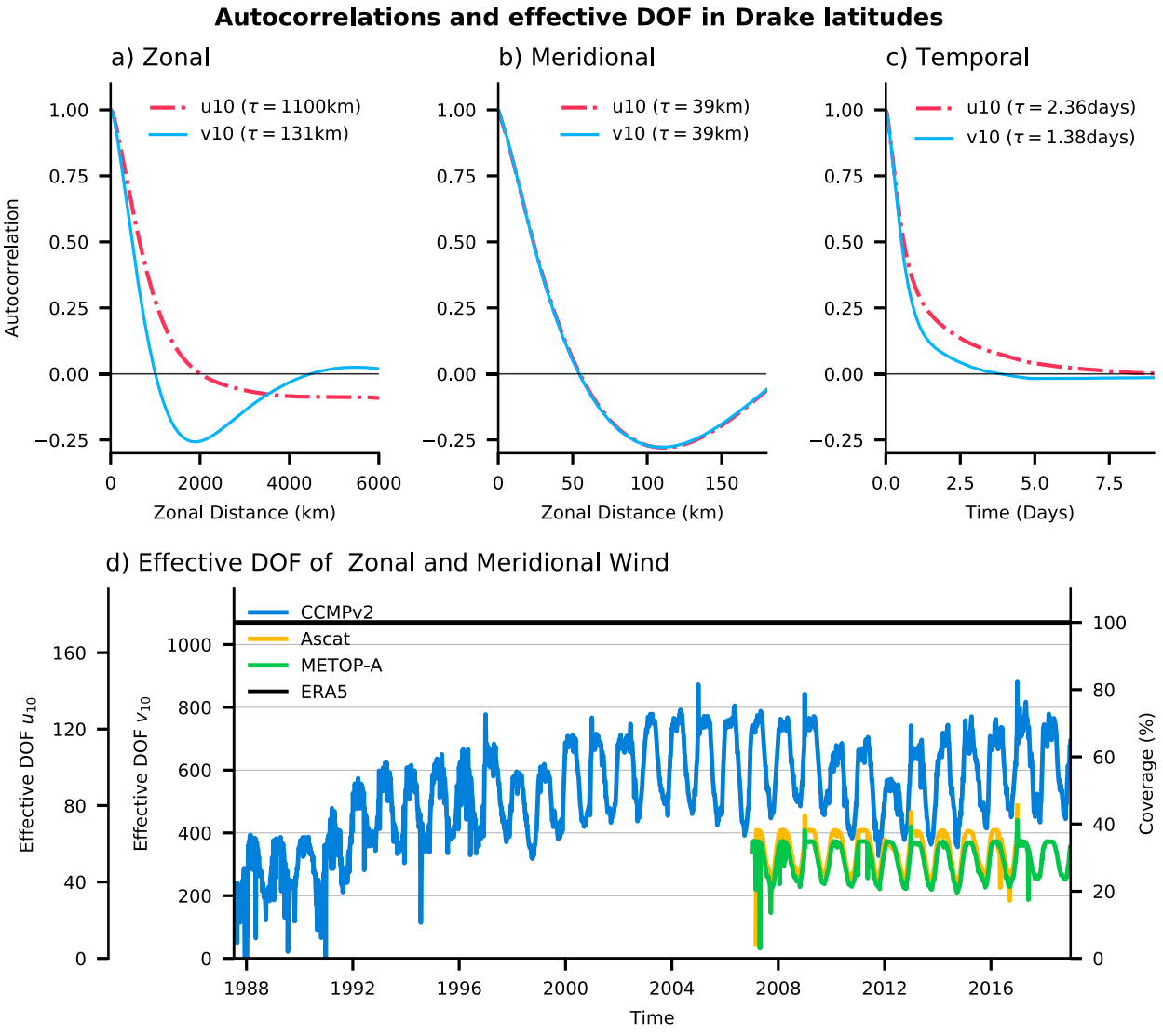

FIG. B1. Autocorrelations and time scales for zonal (red dash-dotted) and meridional wind (light blue) in the (a) zonal and (b) meridional direction, as well as (c) time. (d) Effective degrees of freedom (DOF) and coverage for ERA5 (black), CCMPv2 (blue), ASCAT (red), and *MetOp-A* ASCAT (orange).

1/12 for the twice-daily RSS ASCAT and *MetOp-A* ASCAT data. Figure B1d shows the effective DOF for u_{10}^{PDF} and v_{10}^{PDF} as well as their spatial coverage as a function of time for all four data products. (ERA5 is assumed to provide 100% coverage. The u_{10}^{PDF} and v_{10}^{PDF} DOF have a fixed ratio of about 6.)

APPENDIX C

Southern Annular Mode

The southern annular mode (SAM) is derived from hourly zonal-mean ERA5 zonal wind data that are averaged to 5-day means (Hersbach et al. 2018b). We closely follow Thompson and Woodworth (2013) by first deriving the seasonal anomalies for each 5-day period between 1000 and 50 hPa from 1979 to 2017 at each grid point. The seasonal anomalies are weighted by the square root of the cosine of latitude and by mass, while the latter is estimated from the pressure levels prior to performing the SVD (Thompson and Wallace 2000). Figure C1 shows the results of the SVD of the zonally averaged zonal wind. The leading-order mode of this decomposition is defined as the southern annular mode in this study. SAM derived from geopotential heights rather from zonal winds leads to a nearly identical mode of of variability, and for this study we chose to use zonal wind because of its direct relation to the zonal momentum equation.

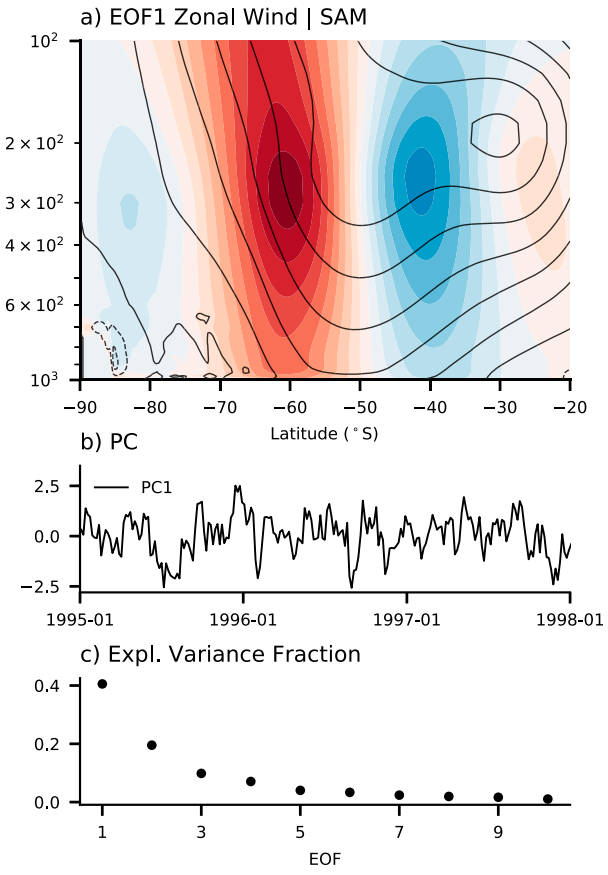

FIG. C1. Southern annular mode decomposition. (a) First EOF of the zonal mean zonal wind between 20°S and 90°S in the troposphere. (b) Example of the corresponding first PC. (c) Explained variance for each mode.

REFERENCES

Ait-Chaalal, F., and T. Schneider, 2014: Why eddy momentum fluxes are concentrated in the upper troposphere. *J. Atmos. Sci.*, **72**, 1585–1604, https://doi.org/10.1175/JAS-D-14-0243.1.

Alford, M. H., 2020: Revisiting near-inertial wind work: Slab models, relative stress, and mixed layer deepening. *J. Phys. Oceanogr.*, **50**, 3141–3156, https://doi.org/10.1175/JPO-D-20-0105.1.

Allen, S., C. A. T. Ferro, and F. Kwasniok, 2020: Recalibrating wind-speed forecasts using regime-dependent ensemble model output statistics. *Quart. J. Roy. Meteor. Soc.*, **146**, 2576–2596, https://doi.org/10.1002/qj.3806.

Andrews, D. G., and M. E. McIntyre, 1976: Planetary waves in horizontal and vertical shear: The generalized Eliassen-Palm relation and the mean zonal acceleration. *J. Atmos. Sci.*, **33**, 2031–2048, https://doi.org/10.1175/1520-0469(1976)033<2031:PWIHAV>2.0.CO;2.

——, and ——, 1978: Generalized Eliassen-Palm and Charney-Drazin theorems for waves on axismmetric mean flows in compressible atmospheres. *J. Atmos. Sci.*, **35**, 175–185, https://doi.org/10.1175/1520-0469(1978)035<0175:GEPACD>2.0.CO;2.

Ardhuin, F., and Coauthors, 2010: Semiempirical dissipation source functions for ocean waves. Part I: Definition, calibration, and validation. *J. Phys. Oceanogr.*, **40**, 1917–1941, https://doi.org/10.1175/2010JPO4324.1.

Asselin, O., and W. R. Young, 2020: Penetration of wind-generated near-inertial waves into a turbulent ocean. *J. Phys. Oceanogr.*, **50**, 1699–1716, https://doi.org/10.1175/JPO-D-19-0319.1.

Atlas, R., R. N. Hoffman, J. Ardizzone, S. M. Leidner, J. C. Jusem, D. K. Smith, and D. Gombos, 2011: A cross-calibrated, multiplatform ocean surface wind velocity product for meteorological and oceanographic applications. *Bull. Amer. Meteor. Soc.*, **92**, 157–174, https://doi.org/10.1175/2010BAMS2946.1.

Belmonte Rivas, M., and A. Stoffelen, 2019: Characterizing ERA-Interim and ERA5 surface wind biases using ASCAT. *Ocean Sci.*, **15**, 831–852, https://doi.org/10.5194/os-15-831-2019.

Bendat, J. S., and A. G. Piersol, 2010: *Random Data: Analysis and Measurement Procedures*. Wiley, 640 pp.

Bengtsson, L., K. I. Hodges, and N. Keenlyside, 2009: Will extratropical storms intensify in a warmer climate? *J. Climate*, **22**, 2276–2301, https://doi.org/10.1175/2008JCLI2678.1.

Bharti, V., C. W. Fairall, B. W. Blomquist, Y. Huang, A. Protat, P. P. Sullivan, S. T. Siems, and M. J. Manton, 2019: Air–sea heat and momentum fluxes in the Southern Ocean. *J. Geophys. Res. Atmos.*, **124**, 12 426–12 443, https://doi.org/10.1029/2018JD029761.

Bidlot, J.-R., D. J. Holmes, P. A. Wittmann, R. Lalbeharry, and H. S. Chen, 2002: Intercomparison of the performance of operational ocean wave forecasting systems with buoy data. *Wea. Forecasting*, **17**, 287–310, https://doi.org/10.1175/1520-0434(2002)017<0287:IOTPOO>2.0.CO;2.

Blackmon, M. L., 1976: A climatological spectral study of the 500 mb geopotential height of the Northern Hemisphere. *J. Atmos. Sci.*, **33**, 1607–1623, https://doi.org/10.1175/1520-0469(1976)033<1607:ACSSOT>2.0.CO;2.

Blein, S., R. Roehrig, A. Voldoire, and G. Faure, 2020: Meso-scale contribution to air–sea turbulent fluxes at GCM scale. *Quart. J. Roy. Meteor. Soc.*, **146**, 2466–2495, https://doi.org/10.1002/qj.3804.

Boé, J., A. Hall, and X. Qu, 2009: Deep ocean heat uptake as a major source of spread in transient climate change simulations. *Geophys. Res. Lett.*, **36**, L22701, https://doi.org/10.1029/2009GL040845.

Böning, C. W., A. Dispert, M. Visbeck, S. R. Rintoul, and F. U. Schwarzkopf, 2008: The response of the Antarctic Circumpolar Current to recent climate change. *Nat. Geosci.*, **1**, 864–869, https://doi.org/10.1038/ngeo362.

Booth, J. F., L. A. Thompson, J. Patoux, K. A. Kelly, and S. Dickinson, 2010: The signature of the midlatitude tropospheric storm tracks in the surface winds. *J. Climate*, **23**, 1160–1174, https://doi.org/10.1175/2009JCLI3064.1.

Bourassa, M. A., and Coauthors, 2013: High-latitude ocean and sea ice surface fluxes: Challenges for climate research. *Bull. Amer. Meteor. Soc.*, **94**, 403–423, https://doi.org/10.1175/BAMS-D-11-00244.1.

——, and Coauthors, 2019: Remotely sensed winds and wind stresses for marine forecasting and ocean modeling. *Front. Mar. Sci.*, **6**, 443, https://doi.org/10.3389/fmars.2019.00443.

Bracegirdle, T. J., and E. W. Kolstad, 2010: Climatology and variability of Southern Hemisphere marine cold-air outbreaks. *Tellus*, **62A**, 202–208, https://doi.org/10.1111/j.1600-0870.2009.00431.x.

Brümmer, B., 1996: Boundary-layer modification in wintertime cold-air outbreaks from the Arctic sea ice. *Bound.-Layer Meteor.*, **80**, 109–125, https://doi.org/10.1007/BF00119014.

Cardone, V. J., R. E. Jensen, D. T. Resio, V. R. Swail, and A. T. Cox, 1996: Evaluation of contemporary ocean wave models in rare extreme events: The "Halloween Storm" of October 1991 and the "storm of the century" of March 1993. *J. Atmos.*

Oceanic Technol., **13**, 198–230, https://doi.org/10.1175/1520-0426(1996)013<0198:EOCOWM>2.0.CO;2.

Catto, J. L., 2018: A new method to objectively classify extratropical cyclones for climate studies: Testing in the southwest Pacific region. *J. Climate*, **31**, 4683–4704, https://doi.org/10.1175/JCLI-D-17-0746.1.

Cavaleri, L., 1994: Applications to wave hindcasting and forecasting. *Dynamics and Modeling of Ocean Waves*, Cambridge University Press, 259–378.

——, 2009: Wave modeling—Missing the peaks. *J. Phys. Oceanogr.*, **39**, 2757–2778, https://doi.org/10.1175/2009JPO4067.1.

——, B. Fox-Kemper, and M. Hemer, 2012: Wind waves in the coupled climate system. *Bull. Amer. Meteor. Soc.*, **93**, 1651–1661, https://doi.org/10.1175/BAMS-D-11-00170.1.

Cerovečki, I., A. J. S. Meijers, M. R. Mazloff, S. T. Gille, V. M. Tamsitt, and P. R. Holland, 2019: The effects of enhanced sea ice export from the Ross Sea on recent cooling and freshening of the southeast Pacific. *J. Climate*, **32**, 2013–2035, https://doi.org/10.1175/JCLI-D-18-0205.1.

Chawla, A., D. M. Spindler, and H. L. Tolman, 2013: Validation of a thirty year wave hindcast using the Climate Forecast System Reanalysis winds. *Ocean Modell.*, **70**, 189–206, https://doi.org/10.1016/j.ocemod.2012.07.005.

Claud, C., A. M. Carleton, B. Duchiron, and P. Terray, 2009: Southern Hemisphere winter cold-air mesocyclones: Climatic environments and associations with teleconnections. *Climate Dyn.*, **33**, 383–408, https://doi.org/10.1007/s00382-008-0468-5.

D'Asaro, E. A., C. C. Eriksen, M. D. Levine, C. A. Paulson, P. Niiler, and P. Van Meurs, 1995: Upper-ocean inertial currents forced by a strong storm. Part I: Data and comparisons with linear theory. *J. Phys. Oceanogr.*, **25**, 2909–2936, https://doi.org/10.1175/1520-0485(1995)025<2909:UOICFB>2.0.CO;2.

Delworth, T. L., and Coauthors, 2012: Simulated climate and climate change in the GFDL CM2.5 high-resolution coupled climate model. *J. Climate*, **25**, 2755–2781, https://doi.org/10.1175/JCLI-D-11-00316.1.

Deser, C., and Coauthors, 2020: Insights from Earth system model initial-condition large ensembles and future prospects. *Nat. Climate Change*, **10**, 277–286, https://doi.org/10.1038/s41558-020-0731-2.

Driesenaar, T., A. Bentamy, J. de Kloe, and M. B. Rivas, 2019: Quality Information Document for the Global Ocean Wind Products. Copernicus Marine Environment Monitoring Service, 11 pp., https://resources.marine.copernicus.eu/documents/QUID/CMEMS-WIND-QUID-012-002-003-005.pdf.

Durrant, T. H., D. J. M. Greenslade, and I. Simmonds, 2013: The effect of statistical wind corrections on global wave forecasts. *Ocean Modell.*, **70**, 116–131, https://doi.org/10.1016/j.ocemod.2012.10.006.

——, ——, ——, and F. Woodcock, 2014: Correcting marine surface winds simulated in atmospheric models using spatially and temporally varying linear regression. *Wea. Forecasting*, **29**, 305–330, https://doi.org/10.1175/WAF-D-12-00101.1.

Edmon, H. J., B. J. Hoskins, and M. E. McIntyre, 1980: Eliassen-Palm cross sections for the troposphere. *J. Atmos. Sci.*, **37**, 2600–2616, https://doi.org/10.1175/1520-0469(1980)037<2600:EPCSFT>2.0.CO;2.

Edson, J. B., and Coauthors, 2013: On the exchange of momentum over the open ocean. *J. Phys. Oceanogr.*, **43**, 1589–1610, https://doi.org/10.1175/JPO-D-12-0173.1.

Fairall, C. W., E. F. Bradley, J. E. Hare, A. A. Grachev, and J. B. Edson, 2003: Bulk parameterization of air–sea fluxes: Updates and verification for the COARE algorithm. *J. Climate*, **16**, 571–591, https://doi.org/10.1175/1520-0442(2003)016<0571:BPOASF>2.0.CO;2.

Feldstein, S., and S. Lee, 1998: Is the atmospheric zonal index driven by an eddy feedback? *J. Atmos. Sci.*, **55**, 3077–3086, https://doi.org/10.1175/1520-0469(1998)055<3077:ITAZID>2.0.CO;2.

Feng, H., D. Vandemark, Y. Quilfen, B. Chapron, and B. Beckley, 2006: Assessment of wind-forcing impact on a global wind-wave model using the TOPEX altimeter. *Ocean Eng.*, **33**, 1431–1461, https://doi.org/10.1016/j.oceaneng.2005.10.015.

Ferrari, R., and C. Wunsch, 2010: The distribution of eddy kinetic and potential energies in the global ocean. *Tellus*, **62A**, 92–108, https://doi.org/10.3402/tellusa.v62i2.15680.

Flato, G., and Coauthors, 2013: Evaluation of climate models. *Climate Change 2013: The Physical Science Basis*, T. F. Stocker et al., Eds., Cambridge University Press, 741–866.

Fletcher, J., S. Mason, and C. Jakob, 2016: The climatology, meteorology, and boundary layer structure of marine cold air outbreaks in both hemispheres. *J. Climate*, **29**, 1999–2014, https://doi.org/10.1175/JCLI-D-15-0268.1.

Gao, L., S. R. Rintoul, and W. Yu, 2018: Recent wind-driven change in Subantarctic Mode Water and its impact on ocean heat storage. *Nat. Climate Change*, **8**, 58–63, https://doi.org/10.1038/s41558-017-0022-8.

George, T., G. Manucharyan, and A. Thompson, 2019: Deep learning to infer eddy heat fluxes from sea surface height patterns of mesoscale turbulence. EarthArXiv, https://eartharxiv.org/repository/view/565/.

Gerber, E. P., and G. K. Vallis, 2007: Eddy–zonal flow interactions and the persistence of the zonal index. *J. Atmos. Sci.*, **64**, 3296–3311, https://doi.org/10.1175/JAS4006.1.

Giglio, D., S. T. Gille, A. C. Subramanian, and S. Nguyen, 2017: The role of wind gusts in upper ocean diurnal variability. *J. Geophys. Res. Oceans*, **122**, 7751–7764, https://doi.org/10.1002/2017JC012794.

Gill, A. E., 1984: On the behavior of internal waves in the wakes of storms. *J. Phys. Oceanogr.*, **14**, 1129–1151, https://doi.org/10.1175/1520-0485(1984)014<1129:OTBOIW>2.0.CO;2.

Gille, S. T., 2005: Statistical characterization of zonal and meridional ocean wind stress. *J. Atmos. Oceanic Technol.*, **22**, 1353–1372, https://doi.org/10.1175/JTECH1789.1.

——, 2008: Decadal-scale temperature trends in the Southern Hemisphere ocean. *J. Climate*, **21**, 4749–4765, https://doi.org/10.1175/2008JCLI2131.1.

Gnanadesikan, A., 1999: A simple predictive model for the structure of the oceanic pycnocline. *Science*, **283**, 2077–2079, https://doi.org/10.1126/science.283.5410.2077.

Grossman, R. L., and A. K. Betts, 1990: Air–sea interaction during an extreme cold air outbreak from the eastern coast of the United States. *Mon. Wea. Rev.*, **118**, 324–342, https://doi.org/10.1175/1520-0493(1990)118<0324:AIDAEC>2.0.CO;2.

Gruber, N., and Coauthors, 2019: The oceanic sink for anthropogenic CO_2 from 1994 to 2007. *Science*, **363**, 1193–1199, https://doi.org/10.1126/science.aau5153.

Haarsma, R. J., and Coauthors, 2016: High Resolution Model Intercomparison Project (High-ResMIP v1.0) for CMIP6. *Geosci. Model Dev.*, **9**, 4185–4208, https://doi.org/10.5194/gmd-9-4185-2016.

Hallberg, R., and A. Gnanadesikan, 2006: The role of eddies in determining the structure and response of the wind-driven Southern Hemisphere overturning: Results from the Modeling Eddies in the Southern Ocean (MESO) project. *J. Phys. Oceanogr.*, **36**, 2232–2252, https://doi.org/10.1175/JPO2980.1.

Hanawa, K., and L. D. Talley, 2001: Mode waters. *Int. Geophys. Ser.*, **77**, 373–386, https://doi.org/10.1016/S0074-6142(01)80129-7.

Hartmann, D. L., and F. Lo, 1998: Wave-driven zonal flow vacillation in the Southern Hemisphere. *J. Atmos. Sci.*, **55**, 1303–1315, https://doi.org/10.1175/1520-0469(1998)055<1303:WDZFVI>2.0.CO;2.

Hasselmann, K., 1976: Stochastic climate models Part I. Theory. *Tellus*, **28**, 473–485, https://doi.org/10.3402/tellusa.v28i6.11316.

Hasselmann, S., and K. Hasselmann, 1985: Computations and parameterizations of the nonlinear energy transfer in a gravity-wave spectrum. Part I: A new method for efficient computations of the exact nonlinear transfer integral. *J. Phys. Oceanogr.*, **15**, 1369–1377, https://doi.org/10.1175/1520-0485(1985)015<1369:CAPOTN>2.0.CO;2.

Haumann, F. A., N. Gruber, M. Münnich, I. Frenger, and S. Kern, 2016: Sea-ice transport driving Southern Ocean salinity and its recent trends. *Nature*, **537**, 89–92, https://doi.org/10.1038/nature19101.

Haynes, P. H., M. E. McIntyre, T. G. Shepherd, C. J. Marks, and K. P. Shine, 1991: On the "downward control" of extratropical diabatic circulations by eddy-induced mean zonal forces. *J. Atmos. Sci.*, **48**, 651–678, https://doi.org/10.1175/1520-0469(1991)048<0651:OTCOED>2.0.CO;2.

Hennessey, J. P., 1977: Some aspects of wind power statistics. *J. Appl. Meteor.*, **16**, 119–128, https://doi.org/10.1175/1520-0450(1977)016<0119:SAOWPS>2.0.CO;2.

Hersbach, H., and Coauthors, 2018a: ERA5 hourly data on single levels from 1979 to present. Copernicus Climate Change Service (C3S) Climate Data Store (CDS). Accessed 1 June 2019, https://doi.org/10.24381/cds.adbb2d47.

——, and Coauthors, 2018b: ERA5 hourly data on pressure levels from 1979 to present. Copernicus Climate Change Service (C3S) Climate Data Store (CDS). Accessed 1 June 2019, https://doi.org/10.24381/cds.bd0915c6.

——, and Coauthors, 2020: The ERA5 global reanalysis. *Quart. J. Roy. Meteor. Soc.*, **146**, 1999–2049, https://doi.org/10.1002/qj.3803.

Holte, J. W., L. D. Talley, T. K. Chereskin, and B. M. Sloyan, 2012: The role of air–sea fluxes in Subantarctic Mode Water formation. *J. Geophys. Res.*, **117**, C03040, https://doi.org/10.1029/2011JC007798.

Hoskins, B. J., and F. P. Bretherton, 1972: Atmospheric frontogenesis models: Mathematical formulation and solution. *J. Atmos. Sci.*, **29**, 11–37, https://doi.org/10.1175/1520-0469(1972)029<0011:AFMMFA>2.0.CO;2.

——, and K. I. Hodges, 2005: A new perspective on Southern Hemisphere storm tracks. *J. Climate*, **18**, 4108–4129, https://doi.org/10.1175/JCLI3570.1.

Huang, F., Z. Xu, and W. Guo, 2020: The linkage between CMIP5 climate models' abilities to simulate precipitation and vector winds. *Climate Dyn.*, **54**, 4953–4970, https://doi.org/10.1007/s00382-020-05259-6.

Janssen, P. A., and J.-R. Bidlot, 2018: Progress in operational wave forecasting. *Procedia IUTAM*, **26**, 14–29, https://doi.org/10.1016/j.piutam.2018.03.003.

Justus, C. G., W. R. Hargraves, A. Mikhail, and D. Graber, 1978: Methods for estimating wind speed frequency distributions. *J. Appl. Meteor.*, **17**, 350–353, https://doi.org/10.1175/1520-0450(1978)017<0350:MFEWSF>2.0.CO;2.

Karoly, D. J., 1990: The role of transient eddies in low-frequency zonal variations of the Southern Hemisphere circulation. *Tellus*, **42A**, 41–50, https://doi.org/10.3402/tellusa.v42i1.11858.

Kay, J. E., and Coauthors, 2015: The Community Earth System Model (CESM) large ensemble project: A community resource for studying climate change in the presence of internal climate variability. *Bull. Amer. Meteor. Soc.*, **96**, 1333–1349, https://doi.org/10.1175/BAMS-D-13-00255.1.

Kuhlbrodt, T., and J. M. Gregory, 2012: Ocean heat uptake and its consequences for the magnitude of sea level rise and climate change. *Geophys. Res. Lett.*, **39**, L18608, https://doi.org/10.1029/2012GL052952.

Li, M., J. Liu, Z. Wang, H. Wang, Z. Zhang, L. Zhang, and Q. Yang, 2013: Assessment of sea surface wind from NWP reanalyses and satellites in the Southern Ocean. *J. Atmos. Oceanic Technol.*, **30**, 1842–1853, https://doi.org/10.1175/JTECH-D-12-00240.1.

Li, Q., A. Webb, B. Fox-Kemper, A. Craig, G. Danabasoglu, W. G. Large, and M. Vertenstein, 2016: Langmuir mixing effects on global climate: WAVEWATCH III in CESM. *Ocean Modell.*, **103**, 145–160, https://doi.org/10.1016/j.ocemod.2015.07.020.

Lim, E.-P., and I. Simmonds, 2007: Southern Hemisphere winter extratropical cyclone characteristics and vertical organization observed with the ERA-40 data in 1979–2001. *J. Climate*, **20**, 2675–2690, https://doi.org/10.1175/JCLI4135.1.

Limpasuvan, V., and D. L. Hartmann, 2000: Wave-maintained annular modes of climate variability. *J. Climate*, **13**, 4414–4429, https://doi.org/10.1175/1520-0442(2000)013<4414:WMAMOC>2.0.CO;2.

Lin, X., X. Zhai, Z. Wang, and D. R. Munday, 2018: Mean, variability, and trend of Southern Ocean wind stress: Role of wind fluctuations. *J. Climate*, **31**, 3557–3573, https://doi.org/10.1175/JCLI-D-17-0481.1.

——, ——, ——, and ——, 2020: Southern Ocean wind stress in CMIP5 models: Role of wind fluctuations. *J. Climate*, **33**, 1209–1226, https://doi.org/10.1175/JCLI-D-19-0466.1.

Lorenz, D. J., and D. L. Hartmann, 2001: Eddy–zonal flow feedback in the Southern Hemisphere. *J. Atmos. Sci.*, **58**, 3312–3327, https://doi.org/10.1175/1520-0469(2001)058<3312:EZFFIT>2.0.CO;2.

Lorenz, E. N., 1967: *The Nature and Theory of the General Circulation of the Atmosphere*. World Meteorological Organization, 161 pp.

Lutsko, N. J., I. M. Held, P. Zurita-Gotor, and A. K. O'Rourke, 2017: Lower-tropospheric eddy momentum fluxes in idealized models and reanalysis data. *J. Atmos. Sci.*, **74**, 3787–3797, https://doi.org/10.1175/JAS-D-17-0099.1.

Maher, N., and Coauthors, 2019: The Max Planck Institute grand ensemble: Enabling the exploration of climate system variability. *J. Adv. Model. Earth Syst.*, **11**, 2050–2069, https://doi.org/10.1029/2019MS001639.

Mbengue, C. O., and T. Woollings, 2019: The eddy-driven jet and storm-track responses to boundary layer drag: Insights from an idealized dry GCM study. *J. Atmos. Sci.*, **76**, 1055–1076, https://doi.org/10.1175/JAS-D-18-0086.1.

McDonald, A. J., and L. H. Cairns, 2020: A new method to evaluate reanalyses using synoptic patterns: An example application in the Ross Sea/Ross Ice Shelf region. *Earth Space Sci.*, **7**, e2019EA000794, https://doi.org/10.1029/2019EA000794.

Meijers, A. J. S., I. Cerovečki, B. A. King, and V. Tamsitt, 2019: A see-saw in Pacific Subantarctic Mode Water formation driven by atmospheric modes. *Geophys. Res. Lett.*, **46**, 13 152–13 160, https://doi.org/10.1029/2019GL085280.

Meredith, M. P., and A. M. Hogg, 2006: Circumpolar response of Southern Ocean eddy activity to a change in the southern annular mode. *Geophys. Res. Lett.*, **33**, L16608, https://doi.org/10.1029/2006GL026499.

——, A. C. Naveira Garabato, A. M. Hogg, and R. Farneti, 2012: Sensitivity of the overturning circulation in the Southern Ocean to decadal changes in wind forcing. *J. Climate*, **25**, 99–110, https://doi.org/10.1175/2011JCLI4204.1.

Miles, J. W., 1960: On the generation of surface waves by turbulent shear flows. *J. Fluid Mech.*, **7**, 469–478, https://doi.org/10.1017/S0022112060000220.

Mizuta, R., and Coauthors, 2017: Over 5,000 years of ensemble future climate simulations by 60-km global and 20-km regional atmospheric models. *Bull. Amer. Meteor. Soc.*, **98**, 1383–1398, https://doi.org/10.1175/BAMS-D-16-0099.1.

Monahan, A. H., 2004: Low-frequency variability of the statistical moments of sea surface winds. *Geophys. Res. Lett.*, **31**, L10302, https://doi.org/10.1029/2004GL019599.

——, 2006a: The probability distribution of sea surface wind speeds. Part I: Theory and SeaWinds observations. *J. Climate*, **19**, 497–520, https://doi.org/10.1175/JCLI3640.1.

——, 2006b: The probability distribution of sea surface wind speeds. Part II: Dataset intercomparison and seasonal variability. *J. Climate*, **19**, 521–534, https://doi.org/10.1175/JCLI3641.1.

——, 2007: Empirical models of the probability distribution of sea surface wind speeds. *J. Climate*, **20**, 5798–5814, https://doi.org/10.1175/2007JCLI1609.1.

——, 2008: Probability distribution of sea surface wind stresses. *Geophys. Res. Lett.*, **35**, L05704, https://doi.org/10.1029/2007GL032268.

——, 2018: Temporal filtering enhances the skewness of sea surface winds. *J. Climate*, **31**, 5695–5706, https://doi.org/10.1175/JCLI-D-17-0814.1.

——, and J. C. Fyfe, 2006: On the nature of zonal jet EOFs. *J. Climate*, **19**, 6409–6424, https://doi.org/10.1175/JCLI3960.1.

——, and ——, 2009: How generic are dipolar jet EOFs? *J. Atmos. Sci.*, **66**, 541–551, https://doi.org/10.1175/2008JAS2814.1.

Naveira Garabato, A. C., L. Jullion, D. P. Stevens, K. J. Heywood, and B. A. King, 2009: Variability of Subantarctic Mode Water and Antarctic Intermediate Water in the Drake Passage during the late-twentieth and early-twenty-first centuries. *J. Climate*, **22**, 3661–3688, https://doi.org/10.1175/2009JCLI2621.1.

Neiman, P. J., and M. A. Shapiro, 1993: The life cycle of an extratropical marine cyclone. Part I: Frontal-cyclone evolution and thermodynamic air–sea interaction. *Mon. Wea. Rev.*, **121**, 2153–2176, https://doi.org/10.1175/1520-0493(1993)121<2153:TLCOAE>2.0.CO;2.

Ogawa, F., and T. Spengler, 2019: Prevailing surface wind direction during air–sea heat exchange. *J. Climate*, **32**, 5601–5617, https://doi.org/10.1175/JCLI-D-18-0752.1.

Ogle, S. E., V. Tamsitt, S. A. Josey, S. T. Gille, I. Cerovečki, L. D. Talley, and R. A. Weller, 2018: Episodic Southern Ocean heat loss and its mixed layer impacts revealed by the farthest south multiyear surface flux mooring. *Geophys. Res. Lett.*, **45**, 5002–5010, https://doi.org/10.1029/2017GL076909.

O'Neill, L. W., D. B. Chelton, and S. K. Esbensen, 2003: Observations of SST-induced perturbations of the wind stress field over the Southern Ocean on seasonal timescales. *J. Climate*, **16**, 2340–2354, https://doi.org/10.1175/2780.1.

——, ——, ——, and F. J. Wentz, 2005: High-resolution satellite measurements of the atmospheric boundary layer response to SST variations along the Agulhas Return Current. *J. Climate*, **18**, 2706–2723, https://doi.org/10.1175/JCLI3415.1.

Osinski, R. D., and H. Radtke, 2020: Ensemble hindcasting of wind and wave conditions with WRF and WAVEWATCH III driven by ERA5. *Ocean Sci.*, **16**, 355–371, https://doi.org/10.5194/os-16-355-2020.

Papritz, L., and S. Pfahl, 2016: Importance of latent heating in mesocyclones for the decay of cold air outbreaks: A numerical process study from the Pacific sector of the Southern Ocean. *Mon. Wea. Rev.*, **144**, 315–336, https://doi.org/10.1175/MWR-D-15-0268.1.

——, ——, H. Sodemann, and H. Wernli, 2015: A climatology of cold air outbreaks and their impact on air–sea heat fluxes in the high-latitude South Pacific. *J. Climate*, **28**, 342–364, https://doi.org/10.1175/JCLI-D-14-00482.1.

Pavia, E. G., and J. J. O'Brien, 1986: Weibull statistics of wind speed over the ocean. *J. Climate Appl. Meteor.*, **25**, 1324–1332, https://doi.org/10.1175/1520-0450(1986)025<1324:WSOWSO>2.0.CO;2.

Peixoto, J. P., and A. H. Oort, 1992: *Physics of Climate*. AIP Press, 520 pp.

Phillips, O. M., 1957: On the generation of waves by turbulent wind. *J. Fluid Mech.*, **2**, 417–445, https://doi.org/10.1017/S0022112057000233.

——, 1985: Spectral and statistical properties of the equilibrium range in wind-generated gravity waves. *J. Fluid Mech.*, **156**, 505–531, https://doi.org/10.1017/S0022112085002221.

Pithan, F., T. G. Shepherd, G. Zappa, and I. Sandu, 2016: Climate model biases in jet streams, blocking and storm tracks resulting from missing orographic drag. *Geophys. Res. Lett.*, **43**, 7231–7240, https://doi.org/10.1002/2016GL069551.

Pollard, R. T., 1980: Properties of near-surface inertial oscillations. *J. Phys. Oceanogr.*, **10**, 385–398, https://doi.org/10.1175/1520-0485(1980)010<0385:PONSIO>2.0.CO;2.

Ponce, S., and F. J. Ocampo-Torres, 1998: Sensitivity of a wave model to wind variability. *J. Geophys. Res.*, **103**, 3179–3201, https://doi.org/10.1029/97JC02328.

Ponte, R. M., and R. D. Rosen, 2004: Nonlinear effects of variable winds on ocean stress climatologies. *J. Climate*, **17**, 1283–1293, https://doi.org/10.1175/1520-0442(2004)017<1283:NEOVWO>2.0.CO;2.

Preisendorfer, R. W., and C. D. Mobley, 1988: *Principal Component Analysis in Meteorology and Oceanography*. Elsevier, 425 pp.

Proistosescu, C., A. Rhines, and P. Huybers, 2016: Identification and interpretation of nonnormality in atmospheric time series. *Geophys. Res. Lett.*, **43**, 5425–5434, https://doi.org/10.1002/2016GL068880.

Ramon, J., L. Lledó, V. Torralba, A. Soret, and F. J. Doblas-Reyes, 2019: What global reanalysis best represents near-surface winds? *Quart. J. Roy. Meteor. Soc.*, **145**, 3236–3251, https://doi.org/10.1002/qj.3616.

Randel, W. J., and I. M. Held, 1991: Phase speed spectra of transient eddy fluxes and critical layer absorption. *J. Atmos. Sci.*, **48**, 688–697, https://doi.org/10.1175/1520-0469(1991)048<0688:PSSOTE>2.0.CO;2.

Rascle, N., F. Ardhuin, P. Queffeulou, and D. Croizé-Fillon, 2008: A global wave parameter database for geophysical applications. Part 1: Wave-current–turbulence interaction parameters for the open ocean based on traditional parameterizations. *Ocean Modell.*, **25**, 154–171, https://doi.org/10.1016/j.ocemod.2008.07.006.

Reimann, L., and J.-S. von Storch, 2020: A phase-space consideration of changing climate-PDF. *Climate Dyn.*, **54**, 2633–2662, https://doi.org/10.1007/s00382-020-05130-8.

Renfrew, I. A., and G. W. K. Moore, 1999: An extreme cold-air outbreak over the Labrador Sea: Roll vortices and air–sea interaction. *Mon. Wea. Rev.*, **127**, 2379–2394, https://doi.org/10.1175/1520-0493(1999)127<2379:AECAOO>2.0.CO;2.

Ribal, A., and I. R. Young, 2020: Calibration and cross validation of global ocean wind speed based on scatterometer

observations. *J. Atmos. Oceanic Technol.*, **37**, 279–297, https://doi.org/10.1175/JTECH-D-19-0119.1.

Ricciardulli, L., and F. J. Wentz, 2016: Remote Sensing Systems ASCAT C-2015 Daily Ocean Vector Winds on 0.25 deg grid, Version 02.1. Remote Sensing Systems, accessed 2 February 2020, www.remss.com/missions/ascat.

Risien, C. M., and D. B. Chelton, 2008: A global climatology of surface wind and wind stress fields from eight years of QuikSCAT scatterometer data. *J. Phys. Oceanogr.*, **38**, 2379–2413, https://doi.org/10.1175/2008JPO3881.1.

Risken, H., 1996: Fokker-Planck equation. *The Fokker-Planck Equation: Methods of Solution and Applications*, H. Risken, Ed., Springer Series in Synergetics, Springer, 63–95, https://doi.org/10.1007/978-3-642-61544-3_4.

Roemmich, D., J. Church, J. Gilson, D. Monselesan, P. Sutton, and S. Wijffels, 2015: Unabated planetary warming and its ocean structure since 2006. *Nat. Climate Change*, **5**, 240–245, https://doi.org/10.1038/nclimate2513.

Rudeva, I., and I. Simmonds, 2015: Variability and trends of global atmospheric frontal activity and links with large-scale modes of variability. *J. Climate*, **28**, 3311–3330, https://doi.org/10.1175/JCLI-D-14-00458.1.

Sabine, C. L., and Coauthors, 2004: The oceanic sink for anthropogenic CO_2. *Science*, **305**, 367–371, https://doi.org/10.1126/science.1097403.

Sallée, J. B., K. G. Speer, and S. R. Rintoul, 2010: Zonally asymmetric response of the Southern Ocean mixed layer depth to the southern annular mode. *Nat. Geosci.*, **3**, 273–279, https://doi.org/10.1038/ngeo812.

Sampe, T., and S.-P. Xie, 2007: Mapping high sea winds from space: A global climatology. *Bull. Amer. Meteor. Soc.*, **88**, 1965–1978, https://doi.org/10.1175/BAMS-88-12-1965.

Schemm, S., and H. Wernli, 2014: The linkage between the warm and the cold conveyor belts in an idealized extratropical cyclone. *J. Atmos. Sci.*, **71**, 1443–1459, https://doi.org/10.1175/JAS-D-13-0177.1.

Schneider, N., 2020: Scale and Rossby number dependence of observed wind responses to ocean-mesoscale sea surface temperatures. *J. Atmos. Sci.*, **77**, 3171–3192, https://doi.org/10.1175/JAS-D-20-0154.1.

Schneider, T., 2006: The general circulation of the atmosphere. *Annu. Rev. Earth Planet. Sci.*, **34**, 655–688, https://doi.org/10.1146/annurev.earth.34.031405.125144.

Schulz, E. W., S. A. Josey, and R. Verein, 2012: First air–sea flux mooring measurements in the Southern Ocean. *Geophys. Res. Lett.*, **39**, L16606, https://doi.org/10.1029/2012GL052290.

Screen, J. A., T. J. Bracegirdle, and I. Simmonds, 2018: Polar climate change as manifest in atmospheric circulation. *Curr. Climate Change Rep.*, **4**, 383–395, https://doi.org/10.1007/s40641-018-0111-4.

Shapiro, M. A., and D. Keyser, 1990: Fronts, jet streams, and the tropopause. *Extratropical Cyclones: The Erik Palmén Memorial Volume*, C. W. Newton and E. Holopainen, Eds., Amer. Meteor. Soc., 167–191.

Shaw, T. A., and Coauthors, 2016: Storm track processes and the opposing influences of climate change. *Nat. Geosci.*, **9**, 656–664, https://doi.org/10.1038/ngeo2783.

——, P. Barpanda, and A. Donohoe, 2018: A moist static energy framework for zonal-mean storm-track intensity. *J. Atmos. Sci.*, **75**, 1979–1994, https://doi.org/10.1175/JAS-D-17-0183.1.

Simmonds, I., 2003: Modes of atmospheric variability over the Southern Ocean. *J. Geophys. Res.*, **108**, 8078, https://doi.org/10.1029/2000JC000542.

——, and M. Dix, 1989: The use of mean atmospheric parameters in the calculation of modeled mean surface heat fluxes over the world's oceans. *J. Phys. Oceanogr.*, **19**, 205–215, https://doi.org/10.1175/1520-0485(1989)019<0205:TUOMAP>2.0.CO;2.

——, and D. A. Jones, 1998: The mean structure and temporal variability of the semiannual oscillation in the southern extratropics. *Int. J. Climatol.*, **18**, 473–504, https://doi.org/10.1002/(SICI)1097-0088(199804)18:5<473::AID-JOC266>3.0.CO;2-0.

——, A. Rafter, T. Cowan, A. B. Watkins, and K. Keay, 2005: Large-scale vertical momentum, kinetic energy and moisture fluxes in the Antarctic sea-ice region. *Bound.-Layer Meteor.*, **117**, 149–177, https://doi.org/10.1007/s10546-004-5939-6.

——, K. Keay, and J. Bye, 2012: Identification and climatology of Southern Hemisphere mobile fronts in a modern reanalysis. *J. Climate*, **25**, 1945–1962, https://doi.org/10.1175/JCLI-D-11-00100.1.

Simpson, I. R., T. G. Shepherd, P. Hitchcock, and J. F. Scinocca, 2013: Southern annular mode dynamics in observations and models. Part II: Eddy feedbacks. *J. Climate*, **26**, 5220–5241, https://doi.org/10.1175/JCLI-D-12-00495.1.

Sinclair, V. A., M. Rantanen, P. Haapanala, J. Räisänen, and H. Järvinen, 2020: The characteristics and structure of extra-tropical cyclones in a warmer climate. *Wea. Climate Dyn.*, **1** (1), 1–25, https://doi.org/10.5194/wcd-1-1-2020.

Small, R. J., R. A. Tomas, and F. O. Bryan, 2014: Storm track response to ocean fronts in a global high-resolution climate model. *Climate Dyn.*, **43**, 805–828, https://doi.org/10.1007/s00382-013-1980-9.

Soloviev, A., and R. Lukas, 2013: *The Near-Surface Layer of the Ocean: Structure, Dynamics and Applications*. Springer, 552 pp.

Song, H., J. Marshall, D. J. McGillicuddy, and H. Seo, 2020: Impact of current–wind interaction on vertical processes in the Southern Ocean. *J. Geophys. Res. Oceans*, **125**, e2020JC016046, https://doi.org/10.1029/2020JC016046.

Song, X., 2020: Explaining the zonal asymmetry in the air–sea net heat flux climatology over the Antarctic Circumpolar Current. *J. Geophys. Res. Oceans*, **125**, e2020JC016215, https://doi.org/10.1029/2020JC016215.

Stopa, J. E., and K. F. Cheung, 2014: Intercomparison of wind and wave data from the ECMWF Reanalysis Interim and the NCEP Climate Forecast System Reanalysis. *Ocean Modell.*, **75**, 65–83, https://doi.org/10.1016/j.ocemod.2013.12.006.

Swart, N. C., S. T. Gille, J. C. Fyfe, and N. P. Gillett, 2018: Recent Southern Ocean warming and freshening driven by greenhouse gas emissions and ozone depletion. *Nat. Geosci.*, **11**, 836–841, https://doi.org/10.1038/s41561-018-0226-1.

Taboada, F. G., C. A. Stock, S. M. Griffies, J. Dunne, J. G. John, R. J. Small, and H. Tsujino, 2019: Surface winds from atmospheric reanalysis lead to contrasting oceanic forcing and coastal upwelling patterns. *Ocean Modell.*, **133**, 79–111, https://doi.org/10.1016/j.ocemod.2018.11.003.

Tamsitt, V., I. Cerovečki, S. A. Josey, S. T. Gille, and E. Schulz, 2020: Mooring observations of air–sea heat fluxes in two Subantarctic Mode Water formation regions. *J. Climate*, **33**, 2757–2777, https://doi.org/10.1175/JCLI-D-19-0653.1.

Tetzner, D., E. Thomas, and C. Allen, 2019: A validation of ERA5 reanalysis data in the southern Antarctic Peninsula—Ellsworth land region, and its implications for ice core studies. *Geosciences*, **9**, 289, https://doi.org/10.3390/geosciences9070289.

Thompson, D. W. J., and J. M. Wallace, 2000: Annular modes in the extratropical circulation. Part I: Month-to-month variability. *J. Climate*, **13**, 1000–1016, https://doi.org/10.1175/1520-0442(2000)013<1000:AMITEC>2.0.CO;2.

——, and S. Solomon, 2002: Interpretation of recent Southern Hemisphere climate change. *Science*, **296**, 895–899, https://doi.org/10.1126/science.1069270.

——, and J. D. Woodworth, 2013: Barotropic and baroclinic annular variability in the Southern Hemisphere. *J. Atmos. Sci.*, **71**, 1480–1493, https://doi.org/10.1175/JAS-D-13-0185.1.

——, and E. A. Barnes, 2014: Periodic variability in the large-scale Southern Hemisphere atmospheric circulation. *Science*, **343**, 641–645, https://doi.org/10.1126/science.1247660.

——, J. M. Wallace, and G. C. Hegerl, 2000: Annular modes in the extratropical circulation. Part II: Trends. *J. Climate*, **13**, 1018–1036, https://doi.org/10.1175/1520-0442(2000)013<1018:AMITEC>2.0.CO;2.

Thompson, K. R., R. F. Marsden, and D. G. Wright, 1983: Estimation of low-frequency wind stress fluctuations over the open ocean. *J. Phys. Oceanogr.*, **13**, 1003–1011, https://doi.org/10.1175/1520-0485(1983)013<1003:EOLFWS>2.0.CO;2.

Thomson, R. E., and W. S. Huggett, 1981: Wind-driven inertial oscillations of large spatial coherence. *Atmos.–Ocean*, **19**, 281–306, https://doi.org/10.1080/07055900.1981.9649116.

Trenberth, K. E., 1991: Storm tracks in the Southern Hemisphere. *J. Atmos. Sci.*, **48**, 2159–2178, https://doi.org/10.1175/1520-0469(1991)048<2159:STITSH>2.0.CO;2.

Trindade, A., M. Portabella, A. Stoffelen, W. Lin, and A. Verhoef, 2020: ERAstar: A high-resolution ocean forcing product. *IEEE Trans. Geosci. Remote Sens.*, **58**, 1337–1347, https://doi.org/10.1109/TGRS.2019.2946019.

Tuller, S. E., and A. C. Brett, 1984: The characteristics of wind velocity that favor the fitting of a Weibull distribution in wind speed analysis. *J. Climate Appl. Meteor.*, **23**, 124–134, https://doi.org/10.1175/1520-0450(1984)023<0124:TCOWVT>2.0.CO;2.

Turner, J., and Coauthors, 1996: The Antarctic First Regional Observing Study of the Troposphere (FROST) project. *Bull. Amer. Meteor. Soc.*, **77**, 2007–2032, https://doi.org/10.1175/1520-0477(1996)077<2007:TAFROS>2.0.CO;2.

Vallis, G. K., 2006: *Atmospheric and Oceanic Fluid Dynamics: Fundamentals and Large-Scale Circulation*. Cambridge University Press, 771 pp.

van Loon, H., 1967: The half-yearly oscillations in middle and high southern latitudes and the coreless winter. *J. Atmos. Sci.*, **24**, 472–486, https://doi.org/10.1175/1520-0469(1967)024<0472:THYOIM>2.0.CO;2.

von Storch, H., and F. W. Zwiers, 1999: *Statistical Analysis in Climate Research*. 1st ed. Cambridge University Press, 484 pp., https://doi.org/10.1017/CBO9780511612336.

Wallace, J. M., G.-H. Lim, and M. L. Blackmon, 1988: Relationship between cyclone tracks, anticyclone tracks and baroclinic waveguides. *J. Atmos. Sci.*, **45**, 439–462, https://doi.org/10.1175/1520-0469(1988)045<0439:RBCTAT>2.0.CO;2.

Wanninkhof, R., 1992: Relationship between wind speed and gas exchange over the ocean. *J. Geophys. Res.*, **97**, 7373–7382, https://doi.org/10.1029/92JC00188.

——, 2014: Relationship between wind speed and gas exchange over the ocean revisited. *Limnol. Oceanogr. Methods*, **12**, 351–362, https://doi.org/10.4319/lom.2014.12.351.

——, S. C. Doney, T. Takahashi, and W. R. McGillis, 2002: The effect of using time-averaged winds on regional air–sea CO_2 fluxes. *Gas Transfer at Water Surfaces*, *Geophys. Monogr.*, Vol. 127, Amer. Geophys. Union, 351–356.

Wen, C., A. Kumar, and Y. Xue, 2019: Uncertainties in reanalysis surface wind stress and their relationship with observing systems. *Climate Dyn.*, **52**, 3061–3078, https://doi.org/10.1007/s00382-018-4310-4.

Wentz, F. J., S. Peteherych, and L. A. Thomas, 1984: A model function for ocean radar cross sections at 14.6 GHz. *J. Geophys. Res.*, **89**, 3689–3704, https://doi.org/10.1029/JC089iC03p03689.

——, R. Scott, R. Hoffman, S. M. Leidner, R. Atlas, and J. Ardizzone, 2015: Remote Sensing Systems Cross-Calibrated Multi-Platform (CCMP) 6-hourly ocean vector wind analysis product on 0.25 deg grid, Version 2.0. Remote Sensing Systems, www.remss.com/measurements/ccmp.

White, C. J., and Coauthors, 2017: Potential applications of subseasonal-to-seasonal (S2S) predictions. *Meteor. Appl.*, **24**, 315–325, https://doi.org/10.1002/met.1654.

Whitt, D. B., S. A. Nicholson, and M. M. Carranza, 2019: Global impacts of subseasonal (<60 day) wind variability on ocean surface stress, buoyancy flux, and mixed layer depth. *J. Geophys. Res. Oceans*, **124**, 8798–8831, https://doi.org/10.1029/2019JC015166.

Xie, J.-H., and J. Vanneste, 2015: A generalised-Lagrangian-mean model of the interactions between near-inertial waves and mean flow. *J. Fluid Mech.*, **774**, 143–169, https://doi.org/10.1017/jfm.2015.251.

Yagi, M., and K. Kutsuwada, 2020: Validation of different global data sets for sea surface wind-stress. *Int. J. Remote Sens.*, **41**, 6022–6049, https://doi.org/10.1080/01431161.2020.1714784.